



Secular Resonances in Nonrestricted Hierarchical Triple Systems

Pan Tan^{1,3,4}, Xiyun Hou^{1,3,4}, Xinhao Liao^{2,3} , Wenlei Wang², and Jingshi Tang^{1,3,4}¹School of Astronomy and Space Science, Nanjing University, Nanjing, 210023, People's Republic of China²Shanghai Astronomical Observatory, Chinese Academy of Science, 200030, People's Republic of China³Institute of Space Environment and Astrodynamics, Nanjing University, Nanjing, 210023, People's Republic of China; houxiyun@nju.edu.cn⁴Key Laboratory of Modern Astronomy and Astrophysics, Ministry of Education, Nanjing, 210023, People's Republic of China

Received 2020 May 15; revised 2020 July 13; accepted 2020 July 16; published 2020 August 28

Abstract

In this paper, the averaged Hamiltonian of a nonrestricted hierarchical triple system truncated at the third order is investigated. First, each secular resonant term is studied. For the well-studied secular quadrupole theory, it is analytically reformulated in a different manner in our work. The resonance width is numerically determined and displayed on the $\sqrt{1 - e_1^2} - \sqrt{1 - e_2^2}$ plane (also denoted as the $\tilde{e}_1 - \tilde{e}_2$ plane). In terms of the octupole terms, we show that for a near-planar configuration of the system, considerable variations of both the eccentricities of the inner and outer orbits can be generated by a single resonant term. The resonance width for every secular resonant angle from the octupole terms is also numerically determined and displayed on the $\tilde{e}_1 - \tilde{e}_2$ plane. The results show that an orbit flip with a near-perpendicular initial mutual inclination is possible for each secular resonance. By displaying the resonance widths of different resonant terms on the same $\tilde{e}_1 - \tilde{e}_2$ plane, we intuitively show the overlap of different secular resonances. Then, the full averaged Hamiltonian with both quadrupole and octupole terms is investigated using the Poincaré surface of section, with a special focus on the orbit flip. For the cases we exploited, we find that the near-planar flip of the inner orbit can be either regular or chaotic while the outer orbit flip is generally chaotic.

Unified Astronomy Thesaurus concepts: [Orbital resonances \(1181\)](#); [Three-body problem \(1695\)](#); [Exoplanet dynamics \(490\)](#); [Celestial mechanics \(211\)](#)

1. Introduction

The nonrestricted hierarchical three-body problem is considered in this paper. The original spatial three-body problem is a Hamiltonian system of nine degrees of freedom (DOF). The implement of the Jacobi frame passes the system to an equivalent six-DOF Hamiltonian system. The hierarchical configuration indicates that the Keplerian motion of two bodies of m_0 and m_1 is perturbed by a third body m_2 , which orbits the inner binary on a much wider orbit. Because the separation between m_0 and m_1 (denoted as r_1) is much smaller than the distance of their barycenter from m_2 (denoted as r_2), the ratio of the separations, i.e., r_1/r_2 , is a small parameter. In this case, the potential function of the system can be expanded as a converged series of r_1/r_2 . For the general three-body problem, the invariable plane can be introduced to eliminate the nodes from the potential function (Deprit 1983) and the system is further reduced to four DOF. In order to study the secular dynamics, the system is then double-averaged to eliminate the fast angles and reduced to two DOF. This process was originally shown by Harrington (1968) for the nonrestricted hierarchical three-body problem, and it was shown that truncated at the second order of the expansion, namely at the quadrupole approximation, the system has one DOF and thus integrable. This integrable system was actually used in an earlier time by Lidov (1962) and Kozai (1962) for the restricted case where the inner body is assumed massless and the outer body moves on a circular orbit. It was shown that the inner test particle's eccentricity and inclination may undergo large oscillations if its inclination is initially large enough. This dynamical behavior is the now well-known Kozai–Lidov mechanism. Vashkov'Yak (1999) and Kinoshita & Nakai (2007) presented the general analytic solutions for the Kozai–Lidov mechanism in the restricted case. For the nonrestricted

case, Lidov & Ziglin (1976) developed a complete quadrupole theory, which analytically investigated the equilibrium points for all permissible values of the system parameters. Ferrer & Osacar (1994) applied the reduction theory to the problem and showed that the reduced phase space is a two-dimensional sphere instead of a cylindrical plane. More recently, Naoz et al. (2013) showed that at the quadrupole approximation, it is possible for the system to oscillate from prograde to retrograde. Martin & Triaud (2016) numerically investigated the behavior of the Kozai–Lidov effects on an inner stellar binary with a planetary mass as the outer third body.

Extending the theory to the third-order truncation of the potential, namely the octupole approximation, people found some new dynamics of the system. Ford et al. (2000) performed a number of numerical integrations to test the validity of the octupole-order secular approximation and found that the inner orbit's eccentricity could grow very close to unity in some cases. Lee & Peale (2003) used both the octupole-level secular perturbation theory and direct numerical orbit integrations to investigate the dynamical evolutions of hierarchical coplanar exoplanetary systems and their variants. Ji et al. (2003) utilized N -body simulations to explore the dynamical evolution of the HD 82943 planetary system, and two mechanisms of stabilizing the system were found, including secular resonance from the octupole terms. Naoz et al. (2011) showed that in a planetary system with two planets orbiting a star, the orbit of the inner planet may flip from prograde to retrograde due to the octupole effects. This finding may help explain the origin of some hot Jupiters (see Dawson & Johnson 2018 for a review) whose orbits are retrograde (e.g., Albrecht et al. 2012). The dynamics arising from the octupole-level approximation is also referred to as the eccentric Kozai–Lidov mechanism and has seen many applications in the

secular evolutions of various natural systems (see Naoz 2016 for a review). In terms of the orbit flip in the restricted hierarchical three-body system where one of the inner bodies is a test particle, Lithwick & Naoz (2011) numerically mapped out the conditions of the orbit flip and the occurrence of extreme eccentricities. Katz et al. (2011) gave an analytical criterion for the flip of the inner orbit with high initial inclination in the restricted case. Li et al. (2014a) investigated the dynamics of the orbit flip of the inner test particle by studying the surfaces of section and the Lyapunov characteristic exponents. Li et al. (2014b) showed that the flip of the inner test particle is even possible starting from a near-planar configuration and derived an analytical criterion for this kind of orbit flip. For the restricted case where the outer body is a test particle, Naoz et al. (2017) showed that the orbit flip of the outer body is also possible when the outer orbit's eccentricity is high with a perpendicular mutual inclination and the dynamics is generally chaotic.

Here, we focus on the secular evolution of the nonrestricted hierarchical three-body system, which is beyond the test particle limit of the restricted problem. The results obtained in the nonrestricted case may be applied to a wider range of natural systems. In this paper, each secular resonant term of the Hamiltonian truncated until the octupole order is first studied. (1) For the quadrupole term, the well-studied secular quadrupole theory is analytically reformulated in a different manner. An analytical criterion for the prograde or retrograde state of the equilibrium point is presented. A necessary but insufficient condition for the orbit to flip is derived. The resonance width is numerically determined and for the first time displayed on the $\tilde{e}_1 - \tilde{e}_2$ plane. When the flip condition is satisfied, an analytical expression for the resonance width is also derived and shows good agreement with the numerical results. (2) In terms of the four octupole secular resonant terms, we show that they can lead to considerable oscillations of the eccentricities of both the inner and the outer orbits for the near-planar configuration of the system. In some cases, the eccentricity can even go from near zero to almost unity and vice versa. The resonance widths for each secular resonant term are numerically determined and displayed on the $\tilde{e}_1 - \tilde{e}_2$ plane. We find that each secular resonance can cause the orbit to periodically flip from prograde to retrograde and vice versa with an initial near-perpendicular configuration of the system. (3) From the numerical results of the resonance width of each secular resonance, we use the overlap criterion to analyze the occurrence of unstable motions due to the interaction of resonances. The predictions by the overlap criterion are verified by the surfaces of section. (4) In the end, using the full averaged Hamiltonian truncated at the octupole order, the near-planar orbit flip in the nonrestricted three-body problem is systematically investigated by studying the surfaces of section. We find that the near-planar flip of the inner orbit can be either regular or chaotic while the outer orbit flip is generally chaotic for the cases we exploited.

2. Model

2.1. Jacobi Coordinate and Harrington's Hamiltonian

Let m_0 and m_1 be the masses of the inner binary and m_2 be the third body orbiting the inner binary on a much wider orbit. In the Jacobi frame, the position vector \mathbf{r}_1 of m_1 is defined to be the vector from m_0 to m_1 and the position vector \mathbf{r}_2 of m_2 is defined as the vector from the mass center of m_0 and m_1 to m_2 .

Starting from Newton's law of universal gravitation, one may obtain the equations of motion for m_1 and m_2 as follows:

$$\begin{aligned} \frac{d^2}{dt^2}\mathbf{r}_1 &= -\frac{\mu_1}{r_1^3}\mathbf{r}_1 + Gm_2\frac{\partial R}{\partial \mathbf{r}_1}, \\ \frac{d^2}{dt^2}\mathbf{r}_2 &= -\frac{\mu_2}{r_2^3}\mathbf{r}_2 + Gm_1\beta\frac{\partial R}{\partial \mathbf{r}_2}, \end{aligned} \quad (1)$$

where G is the gravitational constant, $\mu_1 = G(m_0 + m_1)$, $\mu_2 = G(m_0 + m_1 + m_2)$, $\beta = \frac{m_0(m_0 + m_1 + m_2)}{(m_0 + m_1)^2}$, and R is the common part of the disturbing functions, which is defined as follows

$$R = \sum_{l=2}^{\infty} \alpha_l \frac{r_1^l}{r_2^{l+1}} P_l(\cos \Phi), \quad (2)$$

where Φ is the angle between \mathbf{r}_1 and \mathbf{r}_2 , P_l is the Legendre polynomial of order l , and

$$\alpha_l = \frac{m_0^{l-1} + (-1)^l m_1^{l-1}}{(m_0 + m_1)^{l-1}}. \quad (3)$$

We introduce $\tilde{m}_1 = \frac{m_0 m_1}{m_0 + m_1}$ and $\tilde{m}_2 = \frac{m_2(m_0 + m_1)}{m_0 + m_1 + m_2}$, which are referred to as the reduced masses in classic literatures. It can be easily shown that Equation (1) can be described by the following Hamiltonian:

$$H = -\frac{Gm_0 m_1}{2a_1} - \frac{G(m_0 + m_1)m_2}{2a_2} - \frac{Gm_0 m_1 m_2}{m_0 + m_1} R. \quad (4)$$

Henceforth, we refer to Equation (4) as Harrington's Hamiltonian (Harrington 1968). The canonical variables are defined as

$$\begin{aligned} L_1 &= \tilde{m}_1 \sqrt{\mu_1 a_1} L_2 = \tilde{m}_2 \sqrt{\mu_2 a_2}, \\ G_1 &= L_1 \sqrt{1 - e_1^2} \quad G_2 = L_2 \sqrt{1 - e_2^2}, \\ H_1 &= G_1 \cos i_1 \quad H_2 = G_2 \cos i_2, \end{aligned} \quad (5)$$

where a is the orbit's semimajor axis, e is the orbital eccentricity, i is the orbital inclination, and the subscript i refers to m_1 or m_2 . Throughout this paper $i_1 + i_2$ is also denoted as i_{tot} . The conjugated angle variables l_i , g_i , and h_i stand for the mean anomaly, the argument of perigee, and the longitude of the ascending node of the inner or the outer orbit. Further, we introduce two parameters defined as follows:

$$\alpha = \frac{L_1}{L_2}, \quad \tilde{J} = \frac{\|\mathbf{J}\|}{L_1 + L_2}, \quad (6)$$

where $\mathbf{J} = \mathbf{J}_1 + \mathbf{J}_2$ is an integral of motion, which is the total angular momentum vector of the system.

2.2. Invariable Plane and Some Constraints

It is well known that the ascending nodes can be eliminated from the Hamiltonian if the invariable plane (which is perpendicular to \mathbf{J}) is chosen as the first plane of the reference frame. In this frame, the following constraints can be easily derived (see Appendix A for details):

$$\alpha \sqrt{1 - e_1^2} \sin i_1 = \sqrt{1 - e_2^2} \sin i_2, \quad (7)$$

$$\frac{\alpha}{1+\alpha}\sqrt{1-e_1^2}\cos i_1 + \frac{1}{1+\alpha}\sqrt{1-e_2^2}\cos i_2 = \tilde{J}. \quad (8)$$

More identities can be obtained from Equations (7) and (8) as follows:

$$\cos i_1 = \frac{(1+\alpha)^2\tilde{J}^2 + \alpha^2(1-e_1^2) - (1-e_2^2)}{2\alpha(1+\alpha)\tilde{J}\sqrt{1-e_1^2}}, \quad (9)$$

$$\cos i_2 = \frac{(1+\alpha)^2\tilde{J}^2 - \alpha^2(1-e_1^2) + (1-e_2^2)}{2(1+\alpha)\tilde{J}\sqrt{1-e_2^2}}, \quad (10)$$

$$\cos i_{\text{tot}} = \frac{(1+\alpha)^2\tilde{J}^2 - (1-e_2^2) - \alpha^2(1-e_1^2)}{2\alpha\sqrt{1-e_1^2}\sqrt{1-e_2^2}}, \quad (11)$$

$$\sin i_{\text{tot}} = \frac{(1+\alpha)\tilde{J}}{\sqrt{1-e_2^2}}\sin i_1 = \frac{(1+\alpha)\tilde{J}}{\alpha\sqrt{1-e_1^2}}\sin i_2. \quad (12)$$

These constraints will be used in following studies.

2.3. Literal Expansion

In the reference frame with the invariable plane as the first plane, the relation $\theta = h_1 - h_2 = \pi$ always holds (see Appendix A for details). Substituting $\theta = \pi$ into the expression of $\cos \Phi$, one may obtain

$$\cos \Phi = -\cos u_1 \cos u_2 - \sin u_1 \sin u_2 \cos i_{\text{tot}}, \quad (13)$$

where $u = f + g$ and f is the true anomaly of the orbit. Using the addition theorem of the spherical harmonics, one may obtain

$$P_l(\cos \Phi) = (-1)^l \sum_{m=0}^l (1 + \delta_m) \frac{(l-m)!}{(l+m)!} \times P_l^m(\cos u_1) P_l^m(\cos u_2) \cos(mi_{\text{tot}}), \quad (14)$$

$$\bar{R}_3 = \frac{m_0 - m_1 a_1^3}{m_0 + m_1 a_2^4} \frac{e_2 e_1}{(1-e_2^2)^{5/2}} \times \left(\frac{15}{2048} (4 + 3e_1^2) \left((6 + \cos i_{\text{tot}} + 10 \cos 2i_{\text{tot}} + 15 \cos 3i_{\text{tot}}) \cos(g_1 - g_2) + (6 - \cos i_{\text{tot}} + 10 \cos 2i_{\text{tot}} - 15 \cos 3i_{\text{tot}}) \cos(g_1 + g_2) \right) + \frac{525}{512} e_1^2 \sin^2 i_{\text{tot}} ((1 + \cos i_{\text{tot}}) \cos(3g_1 - g_2) + (1 - \cos i_{\text{tot}}) \cos(3g_1 + g_2)) \right), \quad (21)$$

where

$$\delta_m = \begin{cases} 0, & m = 0 \\ 1, & m \neq 0. \end{cases} \quad (15)$$

From the definition of the associated Legendre polynomial, one may obtain that

$$P_l^m(\cos u_1) = (-1)^m \frac{\sin^m u_1}{2^l l!} \sum_{t=0}^{\lfloor \frac{l-m}{2} \rfloor} \binom{l}{t} \times \frac{(2l-2t)!}{(l-2t-m)!} (-1)^t (\cos u_1)^{l-m-2t}, \quad (16)$$

where $\lfloor \cdot \rfloor$ means the floor function. Applying the trigonometric identities presented in Kaula (1961) to Equation (16) and rearranging the index in the summation in a similar way as

shown in the same paper, one may obtain that

$$P_l^m(\cos u_1) = j^m \sum_{j_1=0}^{\infty} F_{lmj_1} \exp(j(l-2j_1)u_1), \quad (17)$$

where $\exp(\cdot)$ means the exponential function, $j^2 = -1$, and F_{lmj} is a real function defined as follows:

$$F_{lmj} = \sum_{t=0}^{\min\{j, \lfloor \frac{l-m}{2} \rfloor\}} \frac{(-1)^t}{2^{2l-2t} t!} \binom{l}{t} \frac{(2l-2t)!}{(l-2t-m)!} \times \sum_{d=\max\{0, j-t-m\}}^{\min\{l-m-2t, j-t\}} \binom{m}{j-t-d} \binom{l-m-2t}{d} (-1)^{j-t-d}. \quad (18)$$

Applying Equations (14) and (17) to Equation (2), one may obtain that

$$R = \sum_{l=2}^{\infty} \alpha_l \frac{r_1^l}{r_2^{l+1}} (-1)^l \sum_{m=0}^l \cos mi_{\text{tot}} (1 + \delta_m) \times \frac{(l-m)!}{(l+m)!} \sum_{j_1=0}^{\infty} \sum_{j_2=0}^{\infty} F_{lmj_1} F_{lmj_2} \times \cos((l-2j_1)u_1 - (l-2j_2)u_1). \quad (19)$$

2.4. The Averaged Hamiltonian

The fully expanded disturbing function, Equation (19), is then double-averaged to eliminate the short-period harmonic terms. The double-averaged result of the disturbing function truncated at the third order is as follows:

$$\bar{R}_2 = \frac{a_1^2}{a_2^3} (1-e_2^2)^{-3/2} \left(\left(1 + \frac{3}{2} e_1^2 \right) \left(\frac{1}{4} - \frac{3}{8} \sin^2 i_{\text{tot}} \right) + \frac{15}{16} e_1^2 \sin^2 i_{\text{tot}} \cos 2g_1 \right), \quad (20)$$

where \bar{R}_2 and \bar{R}_3 are referred to as the quadrupole and the octupole terms, respectively. The quadrupole and octupole terms are equivalent to the ones used by Ford et al. (2000) and Naoz (2016). The double-averaged system admits five independent parameters, namely $(m_1, m_2, a_1, a_2, \tilde{J})$. The Hamiltonian, i.e., the energy of the averaged system, can be denoted as $\bar{H} = -C_0(\bar{R}_2 + \bar{R}_3)$ if we ignore the first two constant terms in Equation (4).

The double-averaged system truncated at the octupole order has two DOF, with its Hamiltonian consisting of five phase combinations, namely $2g_1, g_1 - g_2, g_1 + g_2, 3g_1 - g_2, 3g_1 + g_2$, which can be denoted as $\psi_{m,n} = mg_1 - ng_2$. The angle $\psi_{2,0}$ belongs to the quadrupole term, while the rest belongs to the octupole terms.

Throughout this paper, the unit of mass is assumed as the mass of the Sun, i.e., M_{\odot} . The unit of length is the mean

distance of Earth from the Sun, i.e., L_{\oplus} . The unit of time is assumed as $\sqrt{L_{\oplus}^3/GM_{\odot}}$. The mass of the central body is assumed as the unit mass, namely $m_0 = 1$. We also note that the calculations presented in this paper for different system parameters and initial conditions are all conducted in the sense of semianalytical calculations using the RKF7(8) integrator and the averaged Hamiltonian described above.

3. The Quadrupole Term $\psi_{2,0}$

3.1. Equilibrium Points and Level Curves

To start with, we introduce some new variables: $\theta = (1 + \alpha)\tilde{J}$, $\eta = 1 - e_1^2$, $\beta = 1 - e_2^2$ and $\xi = \theta^2 - \beta$, which will be used in this subsection to simplify the formulas. Focusing only on the $\psi_{2,0}$ term by ignoring other secular resonant angles, we have

$$\bar{H}_{2,0} = -\frac{Gm_0m_1}{2a_1} - \frac{G(m_0 + m_1)m_2}{2a_2} - C_0\bar{R}_2, \quad (22)$$

where $C_0 = \frac{Gm_0m_1m_2}{m_0 + m_1}$. Obviously, the Hamiltonian is independent of g_2 , so G_2 is an integral of motion, which is equivalent to the invariance of the outer orbit's eccentricity e_2 . As a result, the Hamiltonian described by Equation (22) has one DOF, and the equations of motion are as follows:

$$\frac{dG_1}{dt} = -C_0\frac{15}{8}\frac{a_1^2}{a_2^3}e_1^2(1 - e_2^2)^{-\frac{3}{2}}\sin^2 i_{\text{tot}} \sin 2g_1, \quad (23)$$

$$\frac{dg_1}{dt} = -C_0\frac{a_1^2}{a_2^3}(1 - e_2^2)^{-\frac{3}{2}} \times \left(\left(\frac{3}{8} - \frac{9}{16}\sin^2 i_{\text{tot}} \right) \left(-\frac{2(1 - e_1^2)}{G_1} \right) - \frac{3}{8} \left(1 + \frac{3}{2}e_1^2 \right) \sin 2i_{\text{tot}} \left(\frac{\cos i_1}{G_1 \sin i_1} \right) + \frac{15}{16} \left(\sin^2 i_{\text{tot}} \left(-\frac{2(1 - e_1^2)}{G_1} \right) + e_1^2 \sin 2i_{\text{tot}} \left(\frac{\cos i_1}{G_1 \sin i_1} \right) \right) \cos 2g_1 \right). \quad (24)$$

From Equation (23), one may see that the stationary point only exists at $g_1 = 0$ or $2g_1 = \pi$. Substituting $g_1 = 0$ into Equation (24), one may obtain the condition satisfied by the equilibrium at $g_1 = 0$ as follows:

$$\sin i_1 + \cos i_2 \sin i_{\text{tot}} = 0. \quad (25)$$

From Equations (12) and (25),

$$\cos i_2 = -\frac{\sqrt{\beta}}{\theta}. \quad (26)$$

Substituting Equation (26) into Equation (8), one may obtain

$$\cos i_1 = \frac{1}{\alpha\sqrt{\eta}} \left(\theta + \frac{\beta}{\theta} \right). \quad (27)$$

Substituting Equation (26) into Equation (10), one may obtain

$$\eta = \frac{\theta^2 + 3\beta}{\alpha^2}. \quad (28)$$

So the location, i.e., the inner orbit's eccentricity, of the equilibrium at $g_1 = 0$ is uniquely determined by Equation (28). We denote this value as η_0 . Because $\cos i_2 \geq -1$ and $\eta \leq 1$,

from Equations (26) and (28), one may obtain that

$$\frac{\sqrt{\beta}}{1 + \alpha} \leq \tilde{J} \leq \frac{\sqrt{\alpha^2 - 3\beta}}{1 + \alpha}, \quad (29)$$

which naturally gives $\alpha \geq 2\sqrt{\beta}$. To allow the existence of the equilibrium at $g_1 = 0$, Equation (29) is the constraint on the system parameters. By Equation (26), $\cos i_2$ is strictly negative, which implies that $i_2 > 90^\circ$ and in the same way one may see that $i_1 < 90^\circ$ from Equation (27). Thus, the system is in retrograde state, i.e., $i_{\text{tot}} > 90^\circ$, for the resonance $g_1 = 0$.

Substituting $2g_1 = \pi$ into Equation (24), one may obtain the condition satisfied by the equilibrium point at $2g_1 = \pi$ as follows:

$$1 - e_1^2 - 5\sin^2 i_{\text{tot}} + (1 + 4e_1^2) \left(\frac{\sin i_{\text{tot}}}{\sin i_1} \cos i_2 \right) = 0. \quad (30)$$

It is not hard to find that Equation (30) is in nature a cubic equation for the variable η and the analytical expression of roots is complicated and in complex form. In fact, Equation (30) can be transformed into a quadratic equation of the variable ξ as follows with the help of the Equations (10)–(12):

$$\left(\frac{5}{\alpha^2} \right) \xi^2 - (8\eta^2)\xi - \eta^2(5\alpha^2 - 8\alpha^2\eta + 12\beta) = 0. \quad (31)$$

The roots of the Equation (31) are simply as follows:

$$\xi_1 = \frac{\alpha^2\eta}{5}(4\eta - \sqrt{\Delta}), \quad (32)$$

$$\xi_2 = \frac{\alpha^2\eta}{5}(4\eta + \sqrt{\Delta}), \quad (33)$$

where $\Delta = (4\eta - 5)^2 + 60\frac{\beta}{\alpha^2} = 16\eta^2 + 5(5 - 8\eta + 12\frac{\beta}{\alpha^2})$.

Obviously, ξ_1 and ξ_2 determine the value of \tilde{J} if e_1 is known for fixed values of system parameters. The simple expressions of ξ_1 and ξ_2 can be used to analytically investigate the properties of the equilibrium point. In fact, we show that (see Appendix B for details) the equilibrium point for the resonance $\psi_{2,0} = \pi$ is in retrograde state when $\tilde{J} < \sqrt{1 - e_2^2}/(1 + \alpha)$ while the equilibrium point for the resonance $\psi_{2,0} = \pi$ is in prograde state when $\tilde{J} > \sqrt{1 - e_2^2}/(1 + \alpha)$. We refer to this relation between the system parameters (e_2 , α , \tilde{J}) and the state of the equilibrium point for the resonance $\psi_{2,0} = \pi$ as the quadrupole criterion for the prograde–retrograde state of equilibrium point. This criterion will be numerically examined later.

Moreover, for fixed values of $(m_1, m_2, a_1, a_2, e_2)$, if $\tilde{J} = \sqrt{1 - e_2^2}/(1 + \alpha)$, then Equation (31) shows that the resonance $\psi_{2,0} = \pi$ admits an equilibrium point at $e_1 = 1$ with

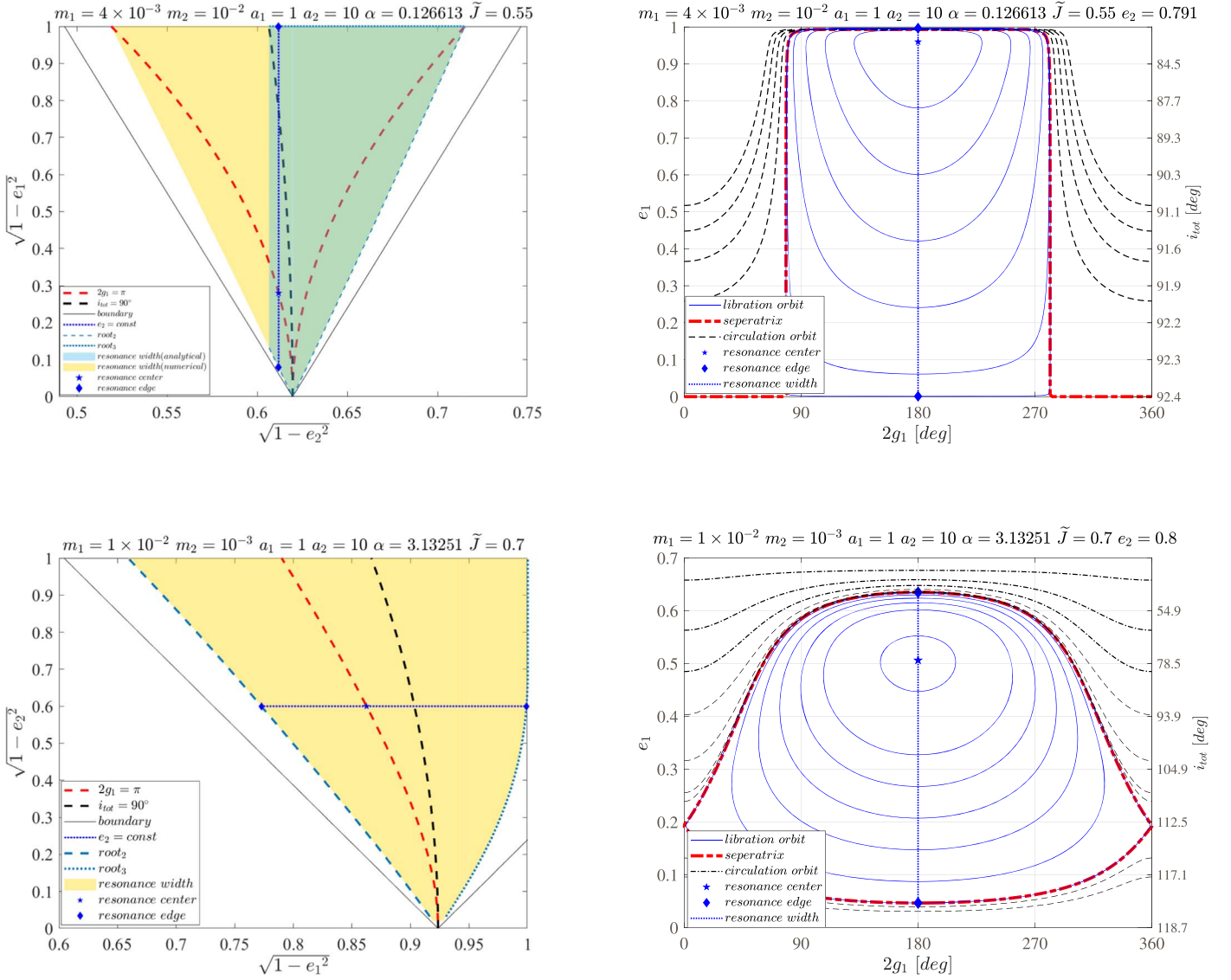


Figure 1. Left: the location of the resonance centers and the resonance width of the quadrupole term on the $\tilde{e}_1 - \tilde{e}_2$ plane for two sets of system parameters. Right: two example level curves described by Equation (35). The resonance width, i.e., the maximum range in which the orbit eccentricity of the inner orbit e_1 can vary is indicated by the vertical blue lines in the right frame. Their corresponding positions in the left frames are also denoted as blue dotted lines. The right ordinate of the right frames is the mutual inclination i_{tot} .

perpendicular mutual inclination, namely $i_{\text{tot}} = 90^\circ$. In fact, we show that (see Appendix C for details)

$$\tilde{J} = \frac{\sqrt{1 - e_2^2}}{1 + \alpha} \Leftrightarrow e_1 = 1 \Leftrightarrow i_1 = 90^\circ \text{ and } i_2 = 0. \quad (34)$$

Equation (34) suggests that the special equilibrium point located at $e_1 = 1$ is uniquely determined by the system parameter $\tilde{J} = \sqrt{1 - e_2^2}/(1 + \alpha)$ or by the perpendicular mutual inclination. Moreover, it has been shown by Lidov & Ziglin (1976) that it is a special equilibrium point and all trajectories will inevitably approach this equilibrium point, i.e., the state $e_1 = 1$. In other words, the system satisfying $\tilde{J} = \sqrt{1 - e_2^2}/(1 + \alpha)$ will experience a collision between m_0 and m_1 in the process of evolution.

The Hamiltonian in Equation (22) has one DOF, so its trajectories are its level curves, which can be numerically computed by choosing different values of $\bar{H}_{2,0}$. Considering the

fact that a_1 , a_2 , and e_2 are constant, an identical way to compute these level curves is by choosing different values of E in the following equation:

$$E = \left(1 + \frac{3}{2}e_1^2\right)\left(\frac{1}{4} - \frac{3}{8}\sin^2 i_{\text{tot}}\right) + \frac{15}{16}e_1^2 \sin^2 i_{\text{tot}} \cos 2g_1. \quad (35)$$

As two examples, the right figures of Figure 1 show how the level curves look like for this resonance. Substituting $g_1 = 0$ into Equation (35), one may obtain that

$$\frac{8}{3}\left(E - \frac{5}{8}\right) = (e_1^2 - 1)(1 + \sin^2 i_{\text{tot}}). \quad (36)$$

With Equations (11) and (36) can be rewritten as

$$\bar{E} = c^2(\eta - \eta_0)^2 - \frac{1 + 2cd}{c^2}, \quad (37)$$

where η_0 is given by Equation (28) and

$$\bar{E} = \frac{8E - 5}{3}, \quad c = \frac{\alpha}{2\sqrt{\beta}} \quad \text{and} \quad d = \frac{\xi}{2\alpha\sqrt{\beta}}. \quad (38)$$

Equation (37) suggests that if $\eta_0 \in (0, 1)$, then the energy E at the point ($g_1 = 0, \eta = \eta_0$) is the minimum along the line $g_1 = 0$ on the phase plane. According to Equation (28), ($g_1 = 0, \eta = \eta_0$) is also the equilibrium point of the system. It is obvious from Equation (35) that the energy E is the maximum along the line $\eta = \eta_0$ on the phase plane. Because the energy at the equilibrium point ($g_1 = 0, \eta = \eta_0$) is not an extremum in its neighborhood, the equilibrium point must be a saddle if it exists.

Substituting $2g_1 = \pi$ into Equation (35), one may obtain that

$$\frac{8}{3} \left(E - \frac{5}{32} \right) = \left(e_1^2 + \frac{1}{4} \right) (1 - 4 \sin^2 i_{\text{tot}}), \quad (39)$$

which is in nature a cubic equation for η and can be solved with the help of Mathematica. One of the three roots of Equation (39) is in the real form and is denoted as root_1 , while the other two are in the complex form and are denoted as root_2 and root_3 (see Appendix D for details). Given a specific Hamiltonian, the maximum and minimum eccentricities along the level curve can be denoted by $e_{1,\text{max}}$ and $e_{1,\text{min}}$. If the orbit flips along the level curve, $\cos i_{\text{tot}}$ must change its sign. Then according to Equation (11), the strict orbit flip criterion is as follows:

$$\xi - \alpha^2(1 - e_{1,\text{max}}^2) > 0, \quad (40)$$

$$\xi - \alpha^2(1 - e_{1,\text{min}}^2) < 0. \quad (41)$$

A necessary but insufficient condition for the orbit to flip at the quadrupole order can be easily derived. First, it is obvious that $\tilde{J} > \sqrt{1 - e_2^2}/1 + \alpha$ is necessary for $\cos i_{\text{tot}}$ to change its sign. Second, substituting $e_{1,\text{min}} = 0$ into Equation (41), we have $\tilde{J} < \sqrt{\alpha^2 + 1 - e_2^2}/1 + \alpha$, so a necessary condition for the orbit to flip is as follows:

$$\frac{\sqrt{1 - e_2^2}}{1 + \alpha} < \tilde{J} < \frac{\sqrt{\alpha^2 + 1 - e_2^2}}{1 + \alpha}. \quad (42)$$

We note that the orbit flip is always possible when Equation (29) is satisfied, because in this case, we have shown that the saddle at $g_1 = 0$ is always in retrograde state and the center at $g_1 = \pi/2$ is always in prograde state.

3.2. Resonance Width

In the above subsection, we have studied the position and stability of the equilibrium points for the resonance $\psi_{2,0}$. According to the studies, we know that the center, i.e., the stable equilibrium point, for the resonance, $\psi_{2,0}$ must be $\psi_{2,0} = \pi$. In this subsection, we display the resonance width in both the numerical and analytical way. For fixed values of ($m_1, m_2, a_1, a_2, \tilde{J}$) and e_2 , level curves of the Hamiltonian by Equation (35) can be easily computed (see the two examples in the right frames of Figure 1). From the level curves, we can separate libration from circulation and determine the resonance width. The separatrix of the resonance can be numerically computed by the condition that $2g_1$ can vary in the entire range

of $[0, 2\pi]$ when the trajectory changes from librational motion to circulatory motion. Further, an analytical expression for the resonance width can be derived when the flip condition, namely Equation (42), is satisfied (see Appendix E for details). Because the orbit eccentricity of the outer orbit e_2 remains unchanged, the resonance width describes the maximum range, namely ($e_{1,\text{min}}, e_{1,\text{max}}$), in which e_1 can vary if the inner orbit is trapped in this resonance. Obviously, for fixed values of ($m_1, m_2, a_1, a_2, \tilde{J}$), the resonance width changes with the value of e_2 . By changing the value of e_2 , we can display the resonance width in the $e_1 - e_2$ plane. As two examples, yellow regions in left frame of Figure 1 displays the numerical result of the resonance width on the $\tilde{e}_1 - \tilde{e}_2$ plane. The reason why we choose this plane instead of the $e_1 - e_2$ plane will be explained later. The result of the analytical approach is presented as the green dashed lines and shows agreement with the numerical result. In the upper-left frame, only a limited range of e_2 is covered by the analytical approach and the result for the resonance width is presented as the green region. In the lower-left frame, the analytical method covers the whole range of e_2 . The red solid curves are the resonance center $2g_1 = \pi$ which can be obtained by solving Equation (30). The boundaries (solid black lines) are determined by Equation (8) with the substitution of ($i_1 = i_2 = 0$), ($i_1 = 0, i_2 = \pi$), and ($i_1 = \pi, i_2 = 0$). As far as we know, this is the first time that the resonance width of the quadrupole term for the non-restricted hierarchical triple system is displayed on such a plane.

The vertical lines in the right frames of Figure 1 passing through the resonance center $2g_1 = \pi$ appear as a blue vertical line in the upper-left frame or the horizontal line in the lower-left frame. The black dashed curves in the left frames are obtained from Equation (11) by setting $i_{\text{tot}} = 90^\circ$. From the left frames, we know that for some values of e_2 , the vertical lines in the upper-left frame or the horizontal lines in the lower-left frame intersect with the dashed black line. This means that the orbital inclination can change from $i_{\text{tot}} < 90^\circ$ to $i_{\text{tot}} > 90^\circ$ and vice versa in one resonant period. This phenomenon, i.e., the orbit flip caused only by the quadrupole term, has already been pointed out by previous researchers (Naos et al. 2013). One remark is that this kind of orbit flip is regular and only happens for values of i_{tot} close to 90° . The necessary condition for the orbit flip to happen is given by Equation (42). Further, it is obvious from Figure 1 that the quadrupole resonance $\psi_{2,0} = \pi$ can lead to considerable variations of the mutual inclination and the inner orbit eccentricity. Generally speaking, when the system is trapped in resonance, the inner orbit eccentricity grows when the mutual inclination decreases and vice versa. The comparison of upper frames and lower frames of Figure 1 also shows that as the value of α grows the maximum range of the oscillation of e_1 decreases while the maximum range of the oscillation of i_{tot} increases.

We note that the upper-left frame of Figure 1 also demonstrates the quadrupole criterion for the prograde-retrograde state of equilibrium point. By definition, the intersection point of $i_{\text{tot}} = 90^\circ$ and $\sqrt{1 - e_1^2} = 0$ is exactly the bifurcation point, i.e., $\tilde{J} = \frac{\sqrt{1 - e_2^2}}{1 + \alpha}$, which is defined in the criterion. The frame shows that the equilibrium points for the resonance $\psi_{2,0} = \pi$ are distributed on both sides of $i_{\text{tot}} = 90^\circ$ and the bifurcation line $\sqrt{1 - e_2^2} = (1 + \alpha)\tilde{J}$. It is obvious that the equilibrium points on the left side of the bifurcation line,

i.e., $\sqrt{1 - e_2^2} = (1 + \alpha)\tilde{J}$ is in prograde state, i.e., $i_{\text{tot}} < 90^\circ$, and the equilibrium points on the right side of the bifurcation line is in retrograde state, i.e., $i_{\text{tot}} > 90^\circ$. This is exactly the statement of the criterion.

4. The Octupole Terms

The octupole terms of the disturbing function consist of four secular resonant angles, namely, $g_1 - g_2$, $g_1 + g_2$, $3g_1 - g_2$, and $3g_1 + g_2$, which can be denoted as $\psi_{m,\pm 1}$. Focusing on one secular resonant term and ignoring others, we apply the canonical transformation by selecting $\psi_{m,\pm 1}$ as the new coordinate. Let the generating function be

$$S_3(g_1, g_2, P_1^*, P_2^*) = (mg_1 \pm g_2)P_1^* + g_2P_2^*, \quad (43)$$

where $(q_1^*, q_2^*, P_1^*, P_2^*)$ are the new conjugated variables. The explicit transformations are as follows

$$\begin{aligned} q_1^* &= mg_1 \pm g_2, \\ q_2^* &= g_2, \\ P_1^* &= G_1, \\ P_2^* &= G_2 \mp \frac{G_1}{m}. \end{aligned}$$

The absence of the variable q_2^* in the Hamiltonian immediately shows that the momentum P_2^* is an integral of motion.

4.1. The Resonance $\Psi_{1,-1}$

4.1.1. Equilibrium Points and Level Curves

Now we consider $\psi_{1,-1}$ as the resonant angle. It is easy to obtain the averaged Hamiltonian as follows:

$$\begin{aligned} \bar{H}_{1,-1} &= -\frac{Gm_0m_1}{2a_1} - \frac{G(m_0 + m_1)m_2}{2a_2} \\ &- C_0 \frac{a_1^2}{a_2^3} (1 - e_2^2)^{-\frac{3}{2}} \left(1 + \frac{3}{2}e_1^2\right) \left(\frac{1}{4} - \frac{3}{8}\sin^2 i_{\text{tot}}\right) \\ &- C_0 \frac{15}{2048} \frac{m_0 - m_1}{m_0 + m_1} \frac{a_1^3}{a_2^4} \frac{e_1 e_2 (4 + 3e_1^2)}{(1 - e_2^2)^{5/2}} \\ &\times (6 + \cos i_{\text{tot}} + 10 \cos 2i_{\text{tot}} + 15 \cos 3i_{\text{tot}}) \\ &\times \cos(g_1 - g_2), \end{aligned} \quad (44)$$

and the equations of motion take the following form:

$$\begin{aligned} \frac{dq_1^*}{dt} &= \frac{\partial \bar{H}_{1,-1}}{\partial G_1}, \\ \frac{dG_1}{dt} &= \frac{\partial \bar{H}_{1,-1}}{\partial q_1^*}. \end{aligned} \quad (45)$$

Equilibrium points require that $dq_1^*/dt = 0$ and $dG_1/dt = 0$ hold at the same time. It is easy to see that the second equation holds when $q_1^* = 0$ or π . Substituting this equality to the first equation, one may obtain the resonance conditions as follows:

$$\frac{dq_1^*}{dt}(e_1, e_2, q_1^* = 0, \alpha, \tilde{J}, P_2^*) = 0, \quad (46)$$

$$\frac{dq_1^*}{dt}(e_1, e_2, q_1^* = \pi, \alpha, \tilde{J}, P_2^*) = 0. \quad (47)$$

Obviously, the integral of motion is $P_2^* = G_2 + G_1$. We introduce a new parameter to replace P_2^* as follows:

$$(\bar{G}_0)_p = \frac{P_2^*}{L_1 + L_2} = \frac{\alpha}{1 + \alpha} \sqrt{1 - e_1^2} + \frac{1}{1 + \alpha} \sqrt{1 - e_2^2}. \quad (48)$$

It is easy to see that $(\bar{G}_0)_p$ is an integral of the motion identical to the integral P_2^* because L_1 and L_2 are constant.

Now we focus on a special situation of the resonance $\psi_{1,-1}$. Notice that the oscillating terms of the original averaged Hamiltonian from Equations (20) and (21) only involve the resonant angle $\psi_{1,-1}$ if $i_{\text{tot}} = 0$. This suggests that the resonance $\psi_{1,-1}$ plays a key role when the system is near-planar and prograde. To put it in a mathematical way, Equation (48), together with Equation (8), shows that when $(\bar{G}_0)_p - \tilde{J} \rightarrow 0$, the system is nearly coplanar and prograde, namely $i_{\text{tot}} \rightarrow 0$. For fixed values of $(m_1, m_2, a_1, a_2, \tilde{J})$ and $(\bar{G}_0)_p$, the location of the equilibrium, i.e., values of e_1 and e_2 , is determined by Equations (46) and (47). Level curves of the Hamiltonian in Equation (44) can be easily computed, and the flows around the equilibrium point on the phase plane show the stability of the equilibrium point. For an example value of $(\bar{G}_0)_p - \tilde{J} = 2 \times 10^{-6}$, the location and stability of the equilibrium points are determined for a wide range of values of α and $(\bar{G}_0)_p$ in Figure 2. We may conclude from Figure 2 that:

- (1) Influenced by the resonance $\psi_{1,-1}$, both the inner and outer orbits' eccentricities vary oppositely due to the conservation constraint given by Equation (48). While both orbits' eccentricities oscillate with the same period, the amplitude of oscillation may differ a lot depending on the system parameters. When α is much smaller than unity ($L_1 \ll L_2$), the inner orbit eccentricity can vary from near zero to almost unity and vice versa, while the outer orbit eccentricity varies in a much smaller range. When α is much larger than unity ($L_1 \gg L_2$), the outer orbit eccentricity can vary from near zero to almost unity, while the inner orbit varies in a much smaller range. When α is close to 1, both inner and outer orbit eccentricities vary considerably.
- (2) For each value of $(\bar{G}_0)_p$, there is at most one equilibrium point for the case of $\psi_{1,-1} = 0$, and this equilibrium is always accompanied by the equilibrium point of $\psi_{1,-1} = \pi$. There are at most three equilibrium points for the case of $\psi_{1,-1} = \pi$ when α is large enough. The equilibrium point for the case of $\psi_{1,-1} = 0$ is always a stable center if it exists. If there is only one equilibrium point of $\psi_{1,-1} = \pi$, it is a stable center. If there are three equilibrium points of $\psi_{1,-1} = \pi$, the one with the middle value of e_1 is unstable while the other two are stable.
- (3) For $\alpha \lesssim 0.3$ ($\alpha \gtrsim 3$) and suitable values of $(\bar{G}_0)_p$, the eccentricity of the inner (outer) orbit can reach almost unity for some initial conditions. We will see that this dynamical behavior is closely related to the near-planar orbit flip.

4.1.2. Resonance Width

In this subsection, we display the resonance width for the resonance $\psi_{1,-1}$. From the level curves presented in Figure 2, we know that the centers for the resonance $\psi_{1,-1}$ are $\psi_{1,-1} = 0$ and

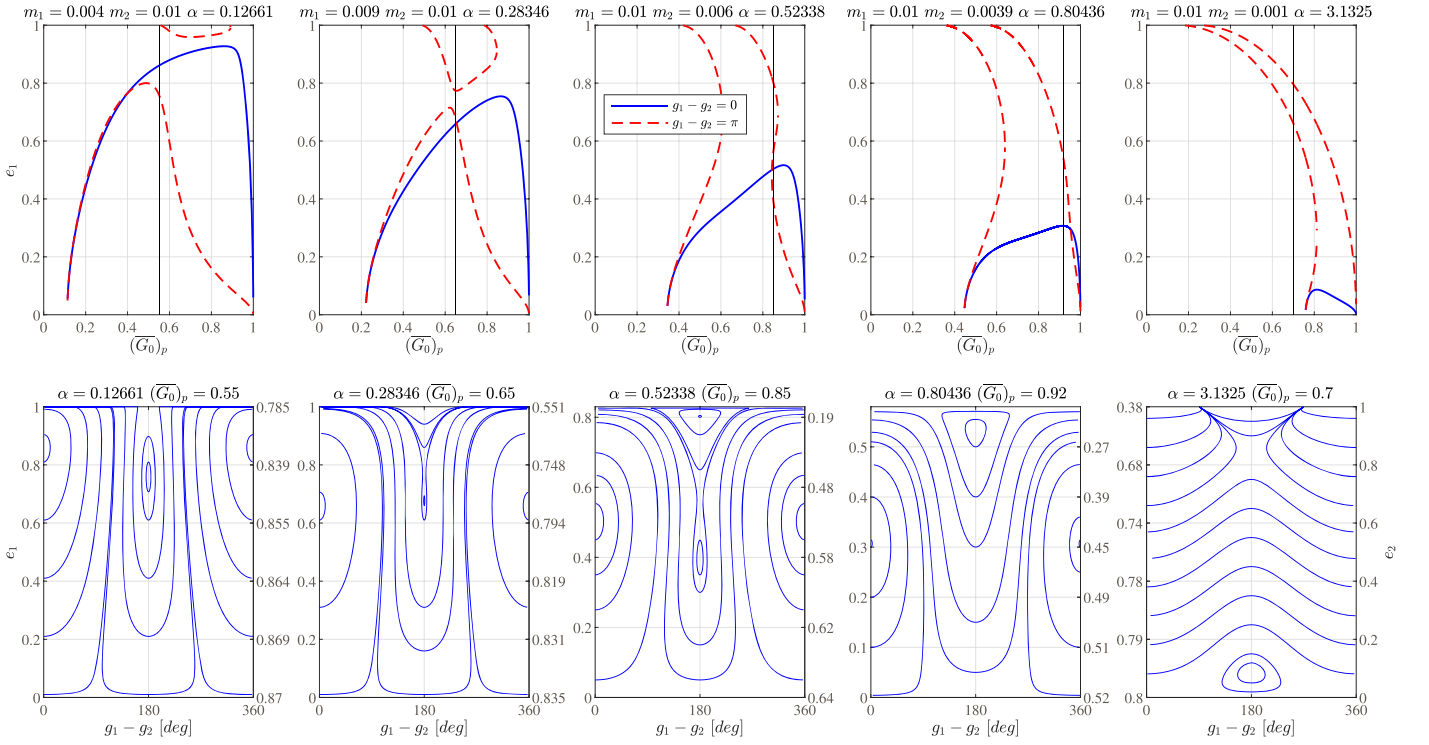


Figure 2. First row: location of the equilibrium points (e_1) of the resonance $\psi_{1,-1}$ for fixed values of system parameters ($m_1, m_2, a_1, a_2, \bar{J}$) and different values of $(\bar{G}_0)_p$. The other system parameters which are not shown in the frame are $a_1 = 1, a_2 = 10$, and $\bar{J} = (\bar{G}_0)_p - 2 \times 10^{-6}$. The example resonance marked by the black vertical line in each frame is investigated in the second row. Second row: the one-DOF phase plane of the example resonance which is marked by the black vertical line in the upper frame in the same column. The left/right ordinates of the lower frames show the inner/outer orbit eccentricity.

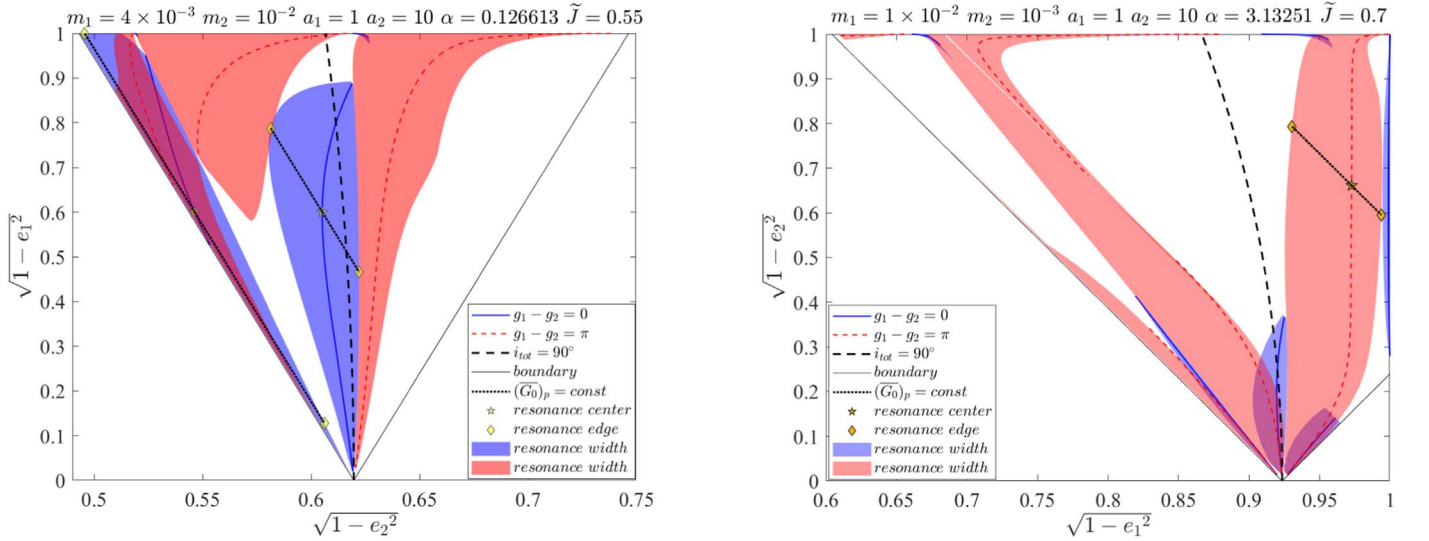


Figure 3. The location of the resonance centers and the resonance width for the resonance $\psi_{1,-1}$ on the $\tilde{e}_1 - \tilde{e}_2$ plane for two sets of system parameters.

$\psi_{1,-1} = \pi$. The separatrix that separates the libration from circulation can be numerically determined as in the case of the resonance $\psi_{2,0}$. The difference of the resonance $\psi_{1,-1}$ is that the integral of motion is $(\bar{G}_0)_p$ instead of e_2 . Because $(\bar{G}_0)_p$ remains unchanged, the feasible range for e_1 , i.e., $(e_{1,\min}, e_{1,\max})$, also determines the feasible range for e_2 , i.e., $(e_{2,\min}, e_{2,\max})$. Therefore, for fixed values of $(m_1, m_2, a_1, a_2, \bar{J})$ and $(\bar{G}_0)_p$, the resonance width for the resonance $\psi_{1,-1}$ is characterized by $(e_{1,\min}, e_{1,\max})$, $(e_{2,\min}, e_{2,\max})$, and $(\bar{G}_0)_p$. From the definition of $(\bar{G}_0)_p$ by

Equation (48), $(\bar{G}_0)_p$ is a linear function of $\sqrt{1 - e_1^2}$ and $\sqrt{1 - e_2^2}$, which implies that $(\bar{G}_0)_p = \text{const}$ is a straight line on the $\tilde{e}_1 - \tilde{e}_2$ plane. Therefore, the resonance width for the resonance $\psi_{1,-1}$ is presented by a segment of the line $(\bar{G}_0)_p = \text{const}$ with two ends at $(\sqrt{1 - e_{1,\max}^2}, \sqrt{1 - e_{2,\min}^2})$ and $(\sqrt{1 - e_{1,\min}^2}, \sqrt{1 - e_{2,\max}^2})$ on the $\tilde{e}_1 - \tilde{e}_2$ plane. As mentioned previously, this is the reason why we choose this plane instead of the $e_1 - e_2$ plane to display the resonance width.

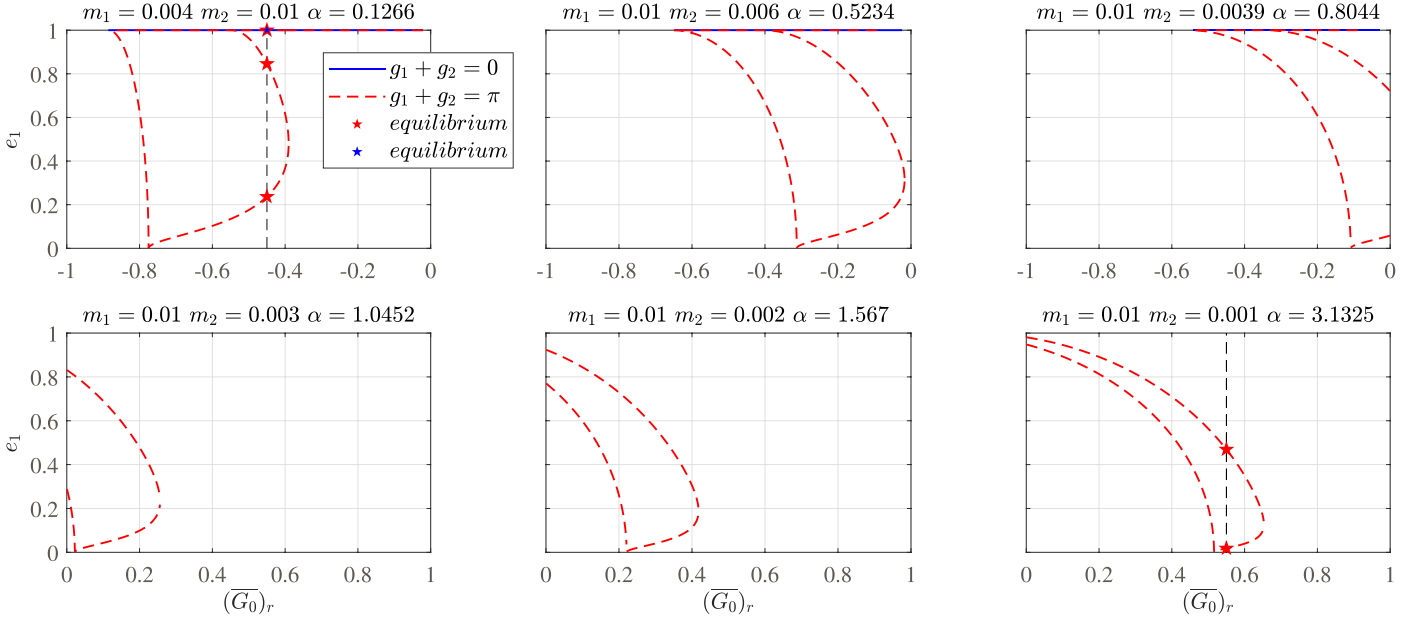


Figure 4. The location of equilibrium points for the resonance $\psi_{1,1}$ for fixed values of $(m_1, m_2, a_1, a_2, \tilde{J})$ and different values of $(\overline{G_0})_r$ for the near-planar retrograde configuration. Blue solid curve: the equilibrium points of $\psi_{1,1} = 0$. Red dashed curve: the equilibrium points of $\psi_{1,1} = \pi$. First row ($i_1 \rightarrow \pi, i_2 \rightarrow 0$): the other system parameters which are not shown in the frames are $a_1 = 1, a_2 = 10$, and $\tilde{J} = -(\overline{G_0})_r + 2 \times 10^{-6}$. Second row ($i_1 \rightarrow 0, i_2 \rightarrow \pi$): the other system parameters which are not shown in the frames are $a_1 = 1, a_2 = 10$ and $\tilde{J} = (\overline{G_0})_r + 2 \times 10^{-6}$.

As two examples, the red and blue regions in Figure 3 display the resonance width around the equilibrium points $\psi_{1,-1} = 0$ and $\psi_{1,-1} = \pi$, respectively. The blue solid curves indicate the equilibrium point of $\psi_{1,-1} = 0$, which can be obtained by solving Equation (46). The red dashed curves indicate the equilibrium points of $\psi_{1,-1} = \pi$, which can be obtained by solving Equation (47). The boundaries and black dashed curves of $i_{\text{tot}} = 90^\circ$ are the same as those in Figure 2. The blue dotted lines passing through the resonance center $\psi_{1,-1} = 0$ or π are examples of the lines given by Equation (48). Their length indicates the resonance width for the chosen value of $(\overline{G_0})_p$. By surveying in the feasible range for the value of $(\overline{G_0})_p$, the blue and red regions in Figure 3 are generated. From the two frames, one remarkable phenomenon is that for some values of $(\overline{G_0})_p$, the blue dotted lines $(\overline{G_0})_p = \text{const}$ intersect with $i_{\text{tot}} = 90^\circ$. This means that the mutual inclination can change from $i_{\text{tot}} < 90^\circ$ to $i_{\text{tot}} > 90^\circ$ and vice versa in one resonant period. This suggests that the resonance $\psi_{1,-1}$ itself can already cause the orbit to periodically flip.

In the previous subsection, we have shown that the inner or outer orbit's eccentricity can reach almost unity. One may see that these resonance centers with near-planar prograde configuration are also demonstrated in Figure 3. To be more specific, in the case of $\alpha \approx 0.1$ in Figure 3, these resonance centers with large resonance widths are located in the leftmost red and blue regions which touch the left border. In the case of $\alpha \approx 3$ in Figure 3, these resonance centers dwell in the leftmost red regions which touch the left border. Further, the right frame of Figure 3 also demonstrates resonance centers with a spatial configuration and large resonance widths that were not studied in the previous subsection. These centers are in the middle-left red region, which extends from top to bottom.

4.2. The Resonance $\Psi_{1,1}$

4.2.1. Equilibrium Points and Level Curves

Now we consider $\psi_{1,1}$ as the resonant angle. It is easy to obtain the averaged Hamiltonian as follows:

$$\begin{aligned} \overline{H}_{1,1} = & -\frac{Gm_0m_1}{2a_1} - \frac{G(m_0 + m_1)m_2}{2a_2} \\ & - C_0 \frac{a_1^2}{a_2^3} (1 - e_2^2)^{-\frac{3}{2}} \left(1 + \frac{3}{2}e_1^2 \right) \left(\frac{1}{4} - \frac{3}{8}\sin^2 i_{\text{tot}} \right) \end{aligned} \quad (49)$$

$$\begin{aligned} & - C_0 \frac{15}{2048} \frac{m_0 - m_1}{m_0 + m_1} \frac{a_1^3}{a_2^4} e_1 e_2 (4 + 3e_1^2) \\ & \times (6 - \cos i_{\text{tot}} + 10 \cos 2i_{\text{tot}} - 15 \cos 3i_{\text{tot}}) \cos(g_1 + g_2), \end{aligned} \quad (50)$$

and equations of motion are as follows:

$$\begin{aligned} \frac{dq_1^*}{dt} &= \frac{\partial \overline{H}_{1,1}}{\partial G_1}, \\ \frac{dG_1}{dt} &= -\frac{\partial \overline{H}_{1,1}}{\partial q_1^*}. \end{aligned} \quad (51)$$

The conditions for the resonance $\psi_{1,1}$ take exactly the same form as Equations (46) and (47). Obviously, the integral of motion is now $P_2^* = G_2 - G_1$. We introduce a new parameter to replace P_2^* as follows:

$$(\overline{G_0})_r = \frac{-P_2^*}{L_1 + L_2} = \frac{\alpha}{1 + \alpha} \sqrt{1 - e_1^2} - \frac{1}{1 + \alpha} \sqrt{1 - e_2^2}. \quad (52)$$

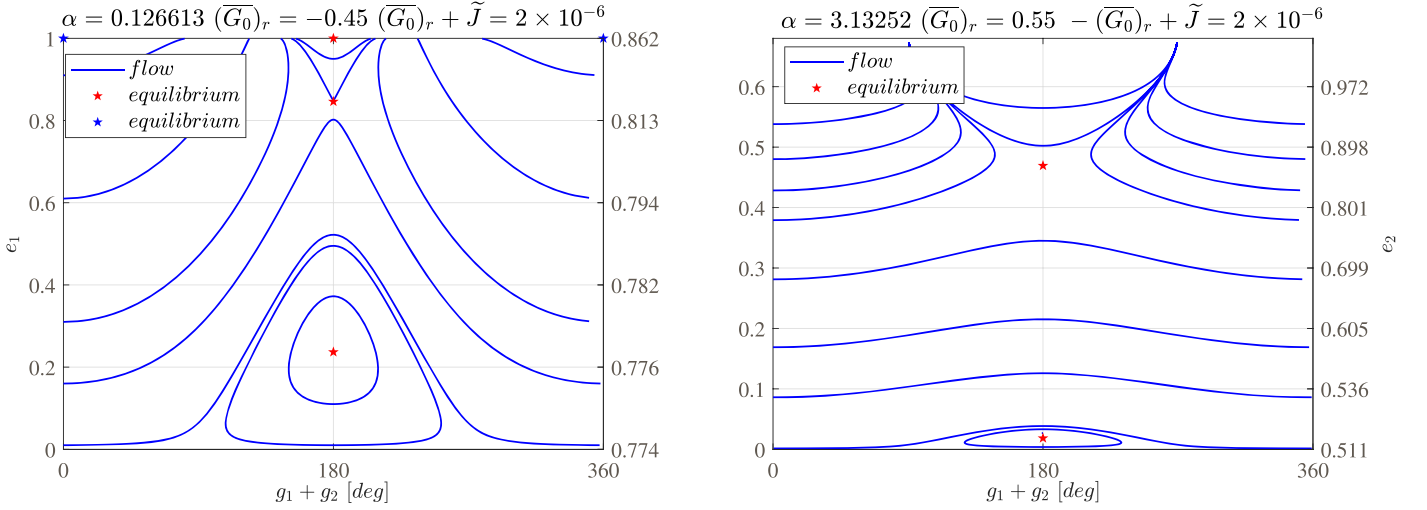


Figure 5. The one-DOF phase plane of two example resonances marked by the vertical dashed line in the upper-left frame and the lower-right frame of Figure 4.

It is easy to see that $(\overline{G_0})_r$ is an integral of motion identical to P_2^* because L_1 and L_2 are constant.

Like the coplanar prograde case for the resonance $\psi_{1,-1}$, we focus on a special situation of the resonance $\psi_{1,1}$. Notice that the oscillating terms of the original averaged Hamiltonian in Equations (20) and (21) only involves the resonant angle $\psi_{1,1}$ if $i_{\text{tot}} = \pi$. This suggests that the resonance $\psi_{1,1}$ dominates when the system is near-planar and retrograde. To put it in a mathematical way, Equation (52) together with Equation (8) shows that when $|(\overline{G_0})_r| + \tilde{J} \rightarrow 0$, the system is near-planar and retrograde, namely, $i_{\text{tot}} \rightarrow \pi$. However, there are two different situations for the near-planar retrograde case, which need separate discussions: $i_1 \rightarrow \pi, i_2 \rightarrow 0$ and $i_1 \rightarrow 0, i_2 \rightarrow \pi$.

- (1) $i_1 \rightarrow \pi, i_2 \rightarrow 0$: because the invariable plane is assumed as the first plane of the reference frame, the inclination of the inner or outer orbit is the angle between \mathbf{J}_1 and \mathbf{J} . Obviously, $i_1 \rightarrow \pi, i_2 \rightarrow 0$ implies that $\|\mathbf{J}_2\| > \|\mathbf{J}_1\|$. In other words, the angular momentum of the outer orbit dominates in this case, which naturally requires an upper limit for the value of α . For an example value of $(\overline{G_0})_r + \tilde{J} = 2 \times 10^{-6}$, the location of the equilibrium point is numerically determined for a wide range of values of α and $(\overline{G_0})_r$. The result is presented in the upper row of Figure 4. Take the value of $(\overline{G_0})_r$ indicated by the vertical line in the upper-left frame as an example. The left frame of Figure 5 shows the level curves for this resonance. The upper row of Figure 4 shows that there exists a center for the resonance $\psi_{1,1} = 0$, which is very close to unity. Depending on the value of $(\overline{G_0})_r$, one or more of the equilibrium points for $\psi_{1,1} = \pi$ may also exist. The left frame of Figure 5 shows that the resonance $\psi_{1,1}$ can lead to considerable oscillation and even to extreme values of e_1 .
- (2) $i_1 \rightarrow 0, i_2 \rightarrow \pi$: in this case, the angular momentum of the inner orbit dominates, which suggests that α has a lower bound. For an example value of $-(\overline{G_0})_r + \tilde{J} = 2 \times 10^{-6}$, the location of the equilibrium point is numerically determined. The result is presented in the lower row of Figure 4. Take the value of $(\overline{G_0})_r$ denoted by the vertical line in the lower-right frame as an example, right frame of Figure 5 shows the level curves for this resonance. The lower row of Figure 4 shows that there exist a center and a

saddle for $\psi_{1,1} = \pi$, but no equilibriums at $\psi_{1,1} = 0$ are identified. The right frame of Figure 5 shows that the resonance $\psi_{1,1}$ can also lead to considerable oscillation and even extreme values of e_2 .

4.2.2. Resonance Width

For the resonance $\psi_{1,1}$, the integral of motion is $(\overline{G_0})_r$, which is also a linear function of $\sqrt{1 - e_1^2}$ and $\sqrt{1 - e_2^2}$. Therefore, it is obvious that the resonance width for the resonance $\psi_{1,1}$ is presented by a segment of the line $(\overline{G_0})_r = \text{const}$ with two ends at $(\sqrt{1 - e_{1,\text{max}}^2}, \sqrt{1 - e_{2,\text{min}}^2})$ and $(\sqrt{1 - e_{1,\text{min}}^2}, \sqrt{1 - e_{2,\text{max}}^2})$ on the $\tilde{e}_1 - \tilde{e}_2$ plane. As two examples, the red and blue regions in Figure 6 display the resonance width around the equilibrium points $\psi_{1,1} = 0$ and $\psi_{1,1} = \pi$, respectively. The blue solid curves are the equilibrium point of $\psi_{1,1} = 0$ while the red dashed curves are the equilibrium point of $\psi_{1,-1} = \pi$. The boundaries and black dashed curves of $i_{\text{tot}} = 90^\circ$ are the same as those in Figure 2. The blue dotted lines passing through the resonance center $\psi_{1,1} = 0$ or π are examples of the lines described by Equation (52). Their length indicates the resonance width for the chosen fixed value of $(\overline{G_0})_r$. From Figure 6, we know that for some values of $(\overline{G_0})_r$, the blue dotted lines $(\overline{G_0})_r = \text{const}$ intersect with the dashed black curve $i_{\text{tot}} = 90^\circ$. This suggests that the resonance $\psi_{1,1}$ alone can also cause the orbit to periodically flip.

4.3. The Resonances $\psi_{3,-1}$ and $\psi_{3,1}$

4.3.1. Equilibrium Points and Level Curves

Now we consider $\psi_{3,-1}$ and $\psi_{3,1}$ as the resonant angles. The averaged Hamiltonians for $\psi_{3,1}$ and $\psi_{3,-1}$ are presented as follows:

$$\begin{aligned}
 \overline{H}_{3,-1} = & -\frac{Gm_0m_1}{2a_1} - \frac{G(m_0 + m_1)m_2}{2a_2} \\
 & - C_0 \frac{a_1^2}{a_2^3} (1 - e_2^2)^{-\frac{3}{2}} \left(1 + \frac{3}{2}e_1^2 \right) \left(\frac{1}{4} - \frac{3}{8}\sin^2 i_{\text{tot}} \right) \\
 & - C_0 \frac{525}{512} \frac{m_0 - m_1}{m_0 + m_1} \frac{a_1^3}{a_2^4} \frac{e_1^3 e_2}{(1 - e_2^2)^{5/2}} \\
 & \times \sin^2 i_{\text{tot}} (1 + \cos i_{\text{tot}}) \cos(3g_1 - g_2),
 \end{aligned} \tag{53}$$

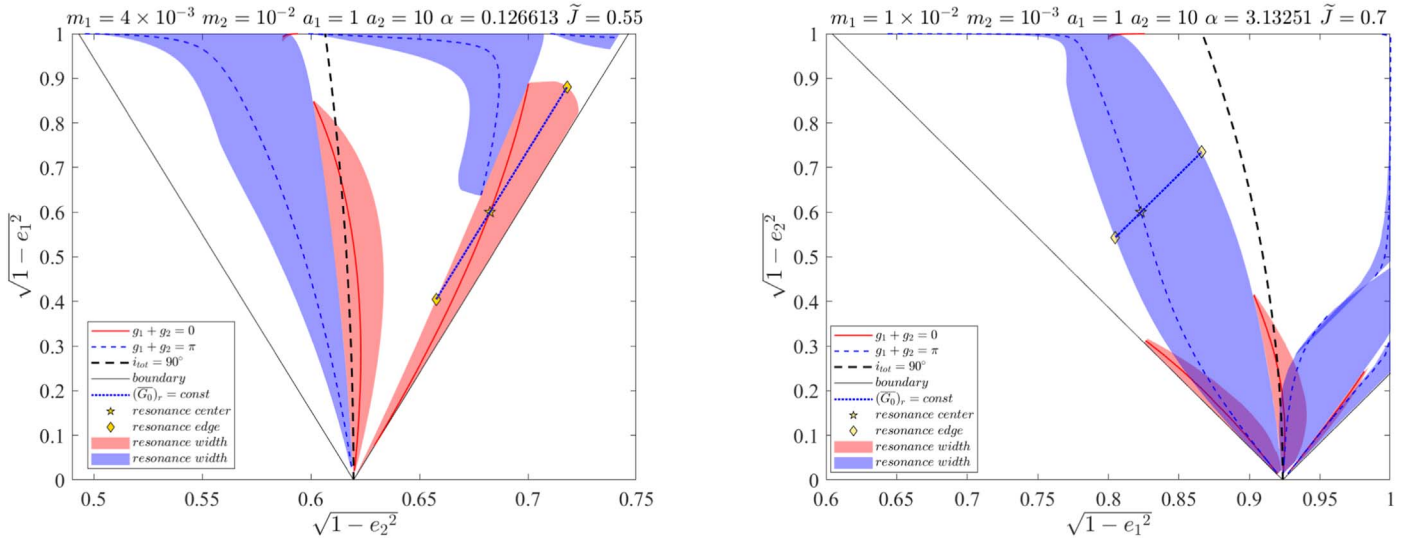


Figure 6. The location of the resonance centers and the resonance width for the resonance $\psi_{1,1}$ on the $\tilde{e}_1 - \tilde{e}_2$ plane for two sets of system parameters.

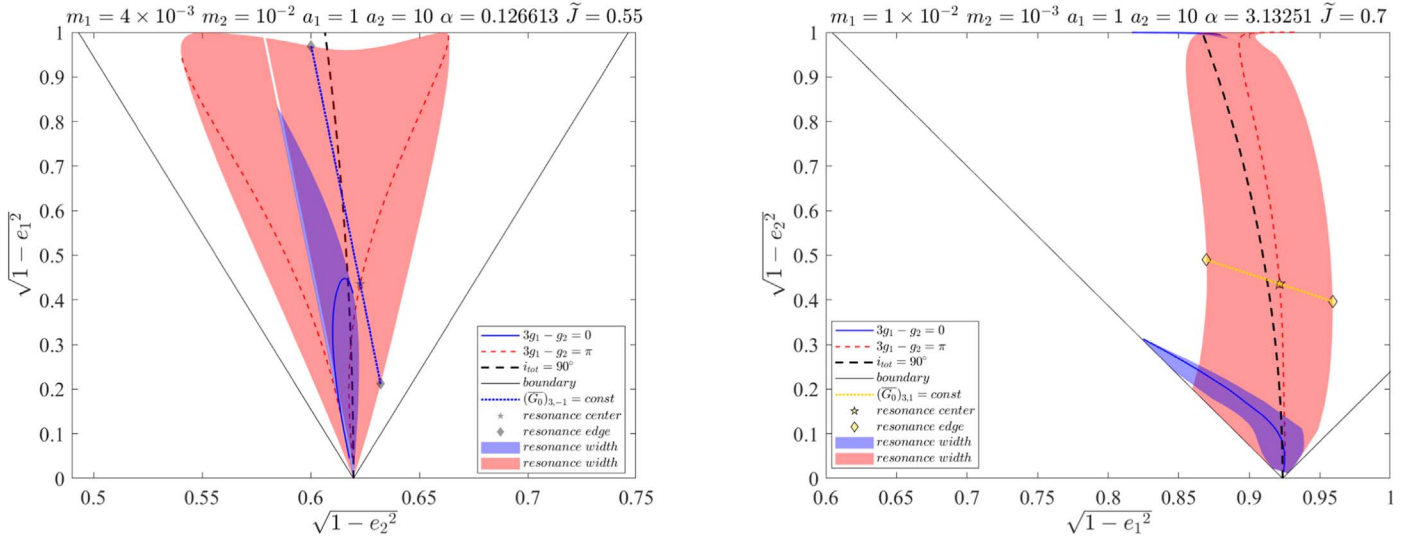


Figure 7. The location of the resonance centers and the resonance width for the resonance $\psi_{3,-1}$ on the $\tilde{e}_1 - \tilde{e}_2$ plane for two sets of system parameters.

$$\begin{aligned}
\bar{H}_{3,1} = & -\frac{Gm_0m_1}{2a_1} - \frac{G(m_0 + m_1)m_2}{2a_2} \\
& - C_0 \frac{a_1^2}{a_2^3} (1 - e_2^2)^{-\frac{3}{2}} \left(1 + \frac{3}{2}e_1^2\right) \left(\frac{1}{4} - \frac{3}{8}\sin^2 i_{\text{tot}}\right) \\
& - C_0 \frac{525 m_0 - m_1 a_1^3}{512 m_0 + m_1 a_2^4} \frac{e_1^3 e_2}{(1 - e_2^2)^{5/2}} \\
& \times \sin^2 i_{\text{tot}} (1 + \cos i_{\text{tot}}) \cos(3g_1 + g_2).
\end{aligned} \tag{54}$$

Notice that the oscillating terms in Equations (53) and (54) both have a factor of e_1^3 , which suggests that the resonance $\psi_{3,-1}$ and $\psi_{3,1}$ are of higher-order magnitude compared to other isolated resonances. Their effects are obvious only when e_1 is large enough. It is obvious that the integrals of motion similar to

those in Equations (48) and (52) are as follows:

$$\begin{aligned}
(\bar{G}_0)_{3,-1} &= \frac{P_2^*}{L_1 + L_2} \\
&= \frac{\alpha}{3(1 + \alpha)} \sqrt{1 - e_1^2} + \frac{1}{1 + \alpha} \sqrt{1 - e_2^2}, \\
(\bar{G}_0)_{3,1} &= \frac{-P_2^*}{L_1 + L_2} \\
&= \frac{\alpha}{3(1 + \alpha)} \sqrt{1 - e_1^2} - \frac{1}{1 + \alpha} \sqrt{1 - e_2^2}.
\end{aligned} \tag{55}$$

For fixed values of $(m_1, m_2, a_1, a_2, \tilde{J})$ and different values of $(\bar{G}_0)_{3,-1}$ ($(\bar{G}_0)_{3,1}$), the location of the equilibrium points and level curves for the resonance $\psi_{3,-1}$ ($\psi_{3,1}$) can be numerically determined using the same method as above. Notice that both

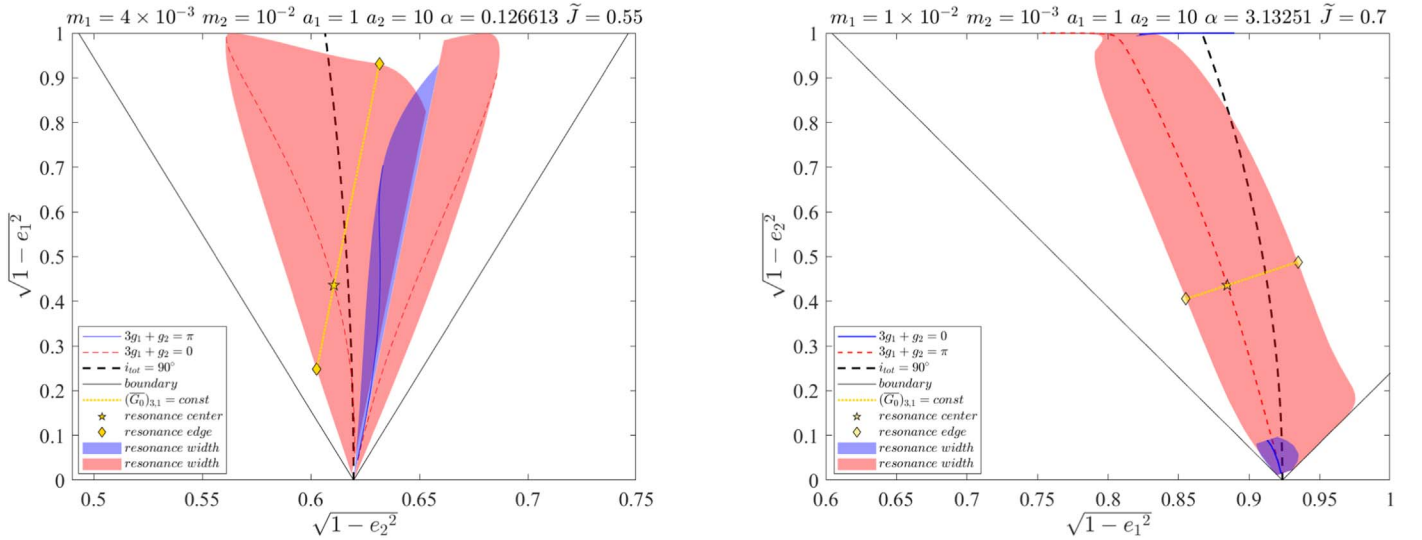


Figure 8. The location of the resonance centers and the resonance width for the resonance $\psi_{3,1}$ on the $\tilde{e}_1 - \tilde{e}_2$ plane for two sets of system parameters.

resonance terms vanish if the system is coplanar, namely $i_{\text{tot}} = 0$ or π . This suggests that a necessary condition for the resonance $\psi_{3,1}$ or $\psi_{3,-1}$ to play its role is a spatial configuration of the system.

4.3.2. Resonance Width

For the resonance $\psi_{3,-1}$ ($\psi_{3,1}$), the corresponding integral of motion $(\overline{G_0})_{3,-1}$ ($(\overline{G_0})_{3,1}$) is also a linear function of $\sqrt{1 - e_1^2}$ and $\sqrt{1 - e_2^2}$. Therefore, the resonance width for the resonance $\psi_{3,-1}$ ($\psi_{3,1}$) can be presented by a segment of the line $(\overline{G_0})_{3,-1} = \text{const}$ ($(\overline{G_0})_{3,1} = \text{const}$) with two ends at $(\sqrt{1 - e_{1,\text{max}}^2}, \sqrt{1 - e_{2,\text{min}}^2})$ and $(\sqrt{1 - e_{1,\text{min}}^2}, \sqrt{1 - e_{2,\text{max}}^2})$ on the $\tilde{e}_1 - \tilde{e}_2$ plane. Figure 7 (Figure 8) shows two examples of the resonance width for the resonance $\psi_{3,-1}$ ($\psi_{3,1}$). The red and blue regions display the resonance width around the equilibrium points $\psi_{3,\pm 1} = 0$ and $\psi_{3,\pm 1} = \pi$, respectively. The blue solid curves indicate the equilibrium point of $\psi_{3,\pm 1} = 0$ while the red dashed curves indicate the equilibrium point of $\psi_{3,\pm 1} = \pi$. The boundaries and black dashed curves of $i_{\text{tot}} = 90^\circ$ are the same as those in Figure 2. The yellow dotted lines passing through the resonance center $\psi_{3,\pm 1} = 0$ or π are examples of the lines described by Equations (55) and (56). Their length indicates the resonance width for the chosen value of $(\overline{G_0})_{3,\pm 1}$.

From Figures 7 and 8, one may see that the equilibrium points for $\psi_{3,1}$ and $\psi_{3,-1}$ are mainly located spatially around the dashed curve $i_{\text{tot}} = 90^\circ$, and they have larger resonance widths when compared with those of $\psi_{1,1}$ and $\psi_{1,-1}$. More importantly, the flip of orbit is possible.

5. Orbit Flip

In the long-term evolution of the hierarchical three-body system, the directions of the orbit planes may exhibit long-term variations due to gravitational interactions. In some cases, the orbit plane of one body may evolve from prograde to retrograde with respect to the total angular momentum vector of the system. This dynamical behavior is known as orbit flip in celestial mechanics. The observations of misaligned hot Jupiters confirmed the possibility of orbit flip in the planetary

systems. Other astrophysical systems, such as triple stars and circumbinary system, are potential candidates for observations of the orbit flip. From the theoretical point of view, this dynamical behavior stems from the secular resonance of the long-term gravitational perturbation and has been studied by many authors in the restricted case (Katz et al. 2011; Lithwick & Naoz 2011; Li et al. 2014a, 2014b; Naoz et al. 2017). In this section, we investigate the inner and the outer orbit flips in the nonrestricted case and especially focus on a special case called the near-planar orbit flip.

5.1. Orbit Flip Caused by a Single Resonance

The above investigation of each of the five secular resonant angles of the Hamiltonian truncated at the octupole level has shown that each single resonance term is capable of periodically flipping the inner or the outer orbit.

At the quadrupole order, we have derived the analytical expression for the resonance width when the flip of the orbit is possible due to the resonance $\psi_{2,0}$. As an example of the inner orbit flip at the quadrupole, the upper-right frame of Figure 1 shows that in the process of the inner orbit flip, the mutual inclination only oscillates around 90° with a small amplitude while the inner orbit eccentricity may vary in $[0, 1]$. As an example of the outer orbit flip at the quadrupole, the lower-right frame of Figure 1 shows that in the process of the outer orbit flip, the mutual inclination can oscillate with a larger amplitude while the oscillation of the inner orbit eccentricity e_1 is confined to a narrow range.

At the octupole order, there are in total four secular resonant angles. To the best of our knowledge, this is the first time that it is shown that each single octupole resonance can periodically flip the orbit. As an example of the inner orbit flip caused by the resonance $\psi_{1,-1}$, the left frame of Figure 9 presents the trajectories on the phase plane to show the oscillation of e_1 and i_{tot} . The blue pentagram marks the location of the resonance center. The resonance width of this center is showed by the black dotted line $(\overline{G_0})_p = \text{const}$ in the left frame of Figure 3. The right frame of Figure 9 presents an example of the inner orbit flip caused by the resonance $\psi_{3,-1}$. The red pentagram marks the location of the resonance center. The resonance width of this center corresponds to the yellow dotted line which

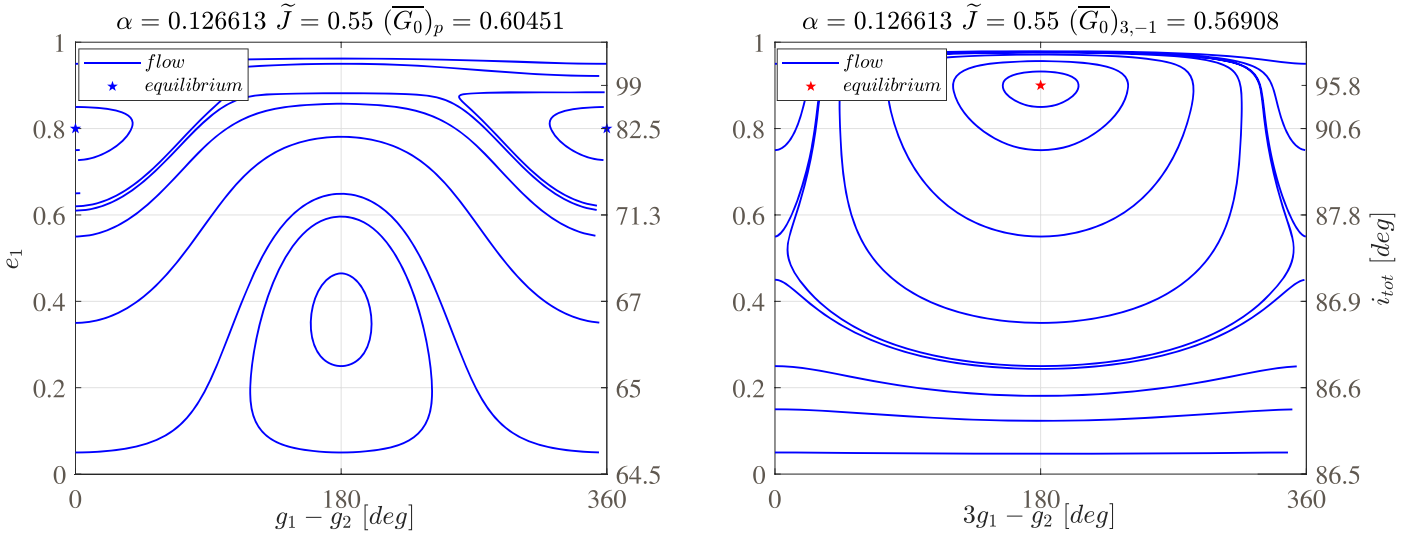


Figure 9. Left: the one-DOF phase plane of an example of the orbit flip caused by the resonance $\psi_{1,-1}$. The other system parameters that are not shown in the frame are the same as those of the left frame of Figure 3. Right: the one-DOF phase plane of an example of the orbit flip caused by the resonance $\psi_{3,-1}$. The other system parameters which are not shown in the frame are the same as those of the left frame of Figure 7.

passes through the resonance center $\psi_{3,-1} = \pi$ in the left frame of Figure 7. These two examples show that the orbit flip caused by a single resonant term from the octupole terms requires a high initial mutual inclination, and the system trapped in resonance is confined to the nearly perpendicular configuration throughout the evolution.

5.2. Near-planar Orbit Flip

In our context, a near-planar orbit flip refers to the inner or the outer orbit flip in the three-body system with an initially near-planar configuration. In other words, the mutual inclination i_{tot} of the system grows from near zero to over 90° in the long-term evolution or vice versa, from nearly 180° to smaller than 90° . The inner near-planar orbit flip was first pointed out by Li et al. (2014b) in the restricted case. In this subsection, we study the near-planar orbit flip in the nonrestricted hierarchical three-body system and investigate the inherent mechanism behind this dynamical behavior. From these studies, we show that the near-planar orbit flip is in nature different from the orbit flip caused by a single resonance. In the case of the near-planar inner orbit flip, it can be either regular or chaotic, while in the case of the outer orbit flip, the motion is generally chaotic.

5.2.1. Three Examples

As a start, we show three examples of the near-planar orbit flip in the nonrestricted hierarchical three-body system (see Figure 10). Examples 1 (left frame) and 2 (middle frame) correspond to the inner orbit flip while example 3 (right frame) corresponds to the outer orbit flip. The intuitive information from the figure is that example 1 is regular while examples 2 and 3 are chaotic.

In the case of example 1, the evolution of the mutual inclination i_{tot} shows that the system quasi-periodically flips from prograde to retrograde and vice versa, and the system can always return to near-planar configuration in the process of flipping. The inner orbit eccentricity e_1 oscillates with the same period as i_{tot} and it can go from 0.4 to almost unity. The evolutions of resonant angles show that $\psi_{1,-1}/\psi_{1,1}$ is in libration when the system is prograde/retrograde. However, neither of the two resonant angles can undergo a complete revolution of libration, which suggests that the

system is not trapped in either of the two resonances. We will show later that this quasi-periodic motion corresponds to a family of invariant tori in the full averaged Hamiltonian.

In the case of example 2, the middle frames of Figure 10 obviously show that the orbit flip is chaotic. To the best of our knowledge, the chaotic inner orbit flip like example 2 has not been pointed out in both the restricted and nonrestricted cases before. The evolution of i_{tot} shows that the system is temporarily confined to the near-planar prograde configuration. The evolution curves of two resonant angles in the corresponding time interval shown in the two middle-lower frames suggest that the system is temporarily trapped in the resonance island $\psi_{1,-1} = \pi$. We will show later that this chaotic flip orbit results from the overlap of different resonance regions.

In the case of example 3, the evolution of mutual inclination shows that the orbit also flips in an unpredictable way, and the evolutions of two resonant angles are both irregular. One may see that the extreme value of the outer orbit's eccentricity e_2 can still be expected at the flip moment. We will show later that this irregularity results from the complicated overlap of multiple resonances.

5.2.2. Resonance Overlap and Chaos

It is well known that resonance overlap leads to chaos (Chirikov 1979). As a result, it is reasonable for us to speculate that the chaos in examples 2 and 3 is caused by the overlap of different secular resonance terms. Figure 11 puts together all five single resonances for the case of the outer orbit flip. The figure tells us that overlap of the resonances is possible, especially when e_2 approaches unity. More specific, the left frame of Figure 11 shows that the red region (resonance width of $\psi_{1,-1}$) overlaps with the blue region (resonance width of $\psi_{1,1}$) while the yellow region (resonance width of $\psi_{2,0}$) serves as a simple background. This suggests that the chaotic motion that migrates between the resonances $\psi_{1,-1}$ and $\psi_{1,1}$ is possible even in the reduced system where only these two resonant angles are considered (a phenomenon we verified but for which no details are shown). The right frame of Figure 11 shows the superimposition of the dark-gray region (resonance widths of $\psi_{3,-1}$ and $\psi_{3,1}$) on the light-gray region (resonance widths of the three resonant terms shown in

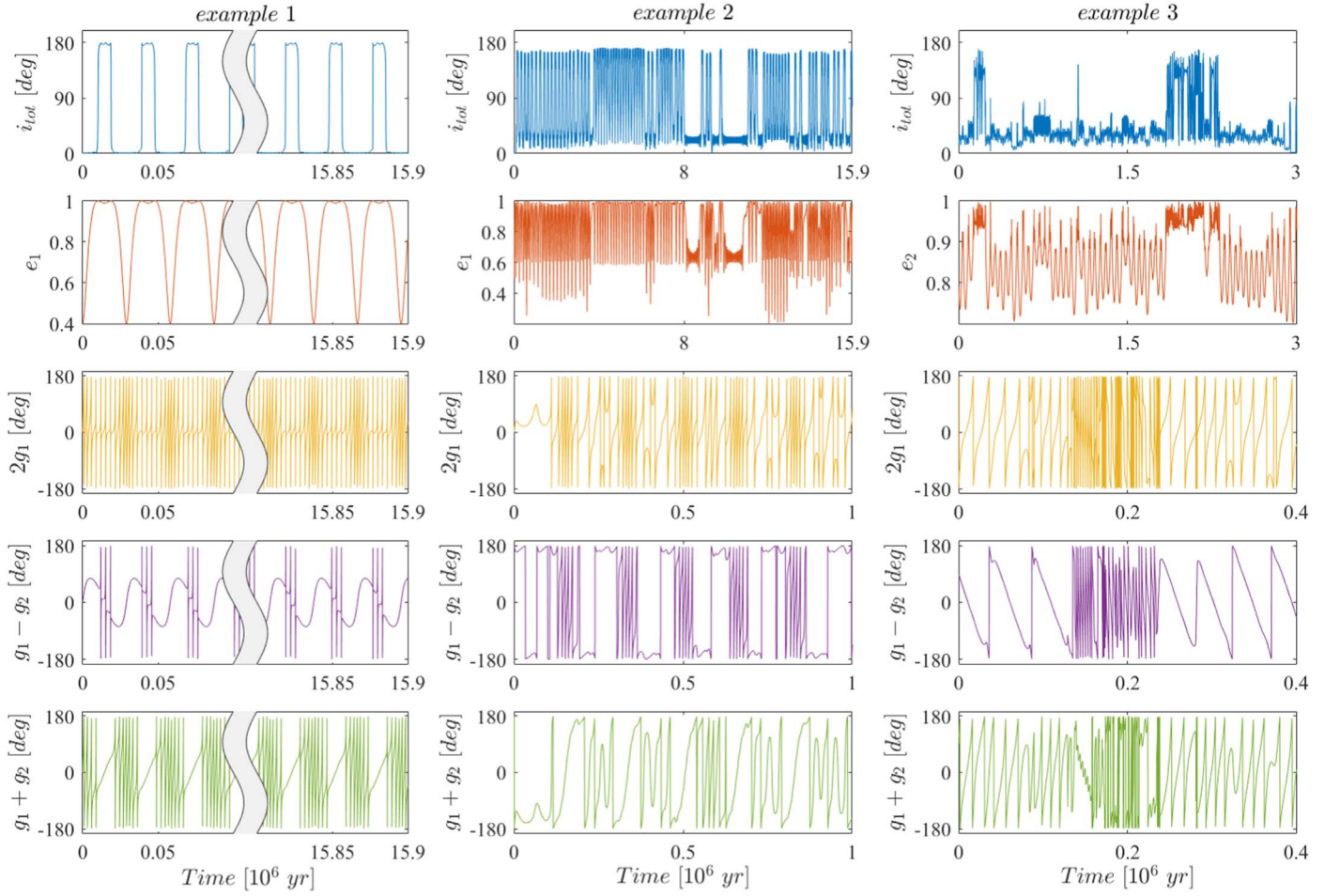


Figure 10. Three examples of a near-planar orbit flip in the nonrestricted hierarchical triple system with the evolutions of the mutual inclination, the eccentricity, and three resonant angles $\psi_{2,0}$, $\psi_{1,-1}$, and $\psi_{1,1}$. The results are obtained by numerical integration of the double-averaged Hamiltonian truncated at the octupole. Left (example 1): the system parameters are $(m_1 = 4 \times 10^{-3}, m_2 = 10^{-2}, a_1 = 1, a_2 = 10, \tilde{J} = 0.55)$. The initial conditions of the trajectory are $(g_{1,0} = 0, g_{2,0} = 0, e_{1,0} = 0.4, e_{2,0} = 0.864)$ with the Hamiltonian $\bar{H} = -1.410 \times 10^{-7}$. Middle (example 2): the system parameters are the same as those of example 1. The initial conditions of the trajectory are $(g_{1,0} = \pi, g_{2,0} = 0, e_{1,0} = 0.5, e_{2,0} = 0.860)$ with the Hamiltonian $\bar{H} = -4.839 \times 10^{-8}$. Right (example 3): the system parameters are $(m_1 = 10^{-2}, m_2 = 10^{-3}, a_1 = 1, a_2 = 10, \tilde{J} = 0.7)$. The initial conditions of the trajectory are $(g_{1,0} = \frac{\pi}{2}, g_{2,0} = 0, e_{1,0} = 0.68, e_{2,0} = 0.79)$ with the Hamiltonian $\bar{H} = -1.554 \times 10^{-8}$.

the left frame). It shows that the resonances $\psi_{3,-1}$ and $\psi_{3,1}$ are mainly distributed around $i_{\text{tot}} = 90^\circ$ and have nonnegligible resonance widths although they are weaker compared to other secular resonant terms.

For the case of the inner orbit flip, Figure 12 puts together all five single resonances in the same way as Figure 11. The left frame of Figure 12 shows that the resonance $\psi_{1,-1}$ overlaps with the resonance $\psi_{1,1}$ around the dashed line $i_{\text{tot}} = 90^\circ$ while the red/blue region that touches the left/right boundary is detached from each other. The overlap around $i_{\text{tot}} = 90^\circ$ means that it is possible for the inner orbit to shift between the resonances $\psi_{1,-1}$ and $\psi_{1,1}$. On the other hand, the detachment between the leftmost and rightmost regions suggests that the motion initially starting from these isolated regions is confined to the corresponding region. In other words, the system with an initial near-planar prograde configuration cannot flip to a near-planar retrograde configuration and vice versa without the help from other resonance terms. The left frame of Figure 12 also shows the resonance width of $\psi_{2,0}$, which is indicated by the yellow region. The yellow region bridges the gap between the leftmost red region and the rightmost blue region. This means that the near-planar orbit flip is possible with the addition of the $\psi_{2,0}$ term (a phenomenon we verified but for which

no details are shown). Similarly, the right frame of Figure 12 shows the resonance regions for $\psi_{3,-1}$ and $\psi_{3,1}$, which also bridge the gap between the leftmost red region and the rightmost blue region. This means that the near-planar inner orbit flip is possible with the addition of these two terms (a phenomenon we verified but for which no details are shown).

5.2.3. Surfaces of Section

The resonance widths in Figures 11 and 12 are plotted by treating each resonance term separately and ignoring the others. In the full averaged Hamiltonian, all five secular resonant terms are present simultaneously, so the phase space is different from the one by simply adding the phase spaces of each resonance term. As a result, the overlap criterion only serves as an intuitive description of their mutual influence. The purpose of Figures 11 and 12 is to intuitively show readers that overlapping of different resonances is widespread in the phase space. In the following, we will use a stricter tool—the surface of section—to study the near-planar orbit flip problem.

The surface of section is initialized by selecting a plane that transversally intersects the three-dimensional energy level

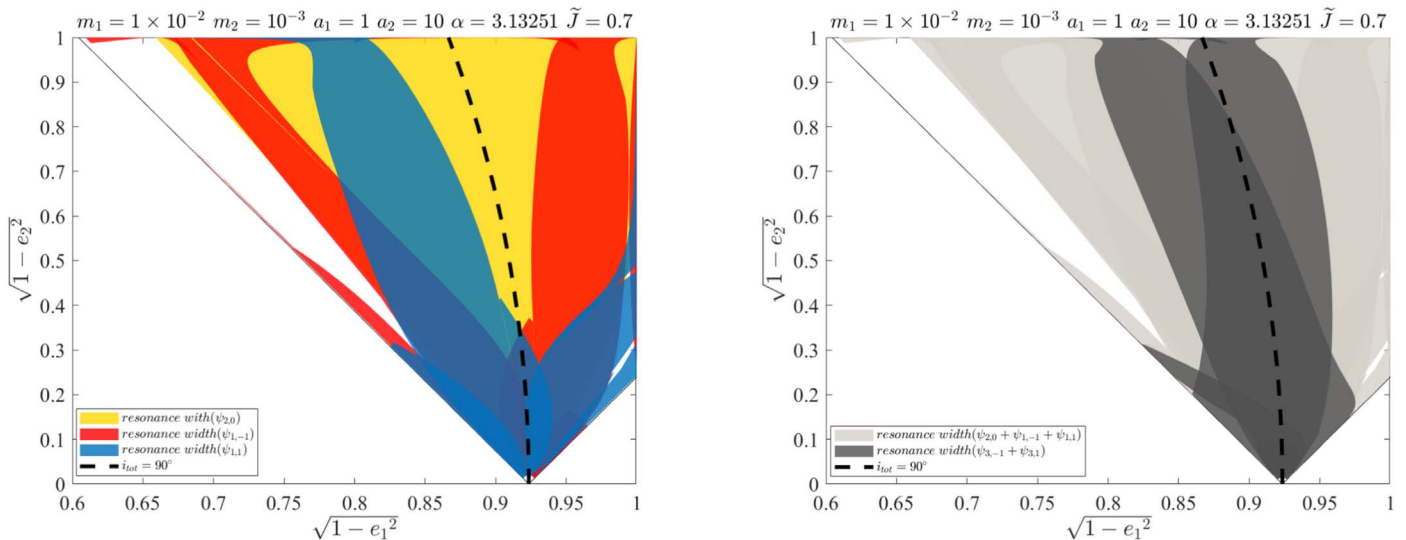


Figure 11. The resonance width of multiple resonances on the $\tilde{e}_1 - \tilde{e}_2$ plane in the case of the outer orbit flip. Left: the yellow region corresponds to the resonance $\psi_{2,0}$ (also see the lower-left frame of Figure 1). The red region corresponds to the resonance $\psi_{1,-1}$ (also see the right frame of Figure 3). The blue region corresponds to the resonance $\psi_{1,1}$ (also see the right frame of Figure 6). Right: the dark-gray regions correspond to the resonances $\psi_{3,-1}$ and $\psi_{3,1}$ which have been presented in the right frames of Figures 7 and 8

manifold. This can be achieved by fixing the value of one of the conjugated coordinates. In the case of the inner/outer orbit flip, the evolutions of two resonant angles g_1 and g_2 show that the sign of \dot{g}_2/\dot{g}_1 changes at the flip moment while \dot{g}_1/\dot{g}_2 remains generally positive. For this reason, we choose the section as $g_1 = 0/g_2 = 0$ in the case of the inner/outer orbit flip.⁵ Each surface is plotted by collecting the intersection points with the section of trajectories with the same energy. By varying the energy, we obtain a series of surfaces that can reveal the structure of the phase space. Generally, a periodic trajectory leaves only finite intersection points on the surface while the intersection points of a quasi-periodic trajectory form a set of regular curves, and the intersection points of a chaotic trajectory seem to be randomly spread on the surface.

The surface presented in frame (a) of Figure 13 has the same energy as example 1, for which the intersection points are marked with red dots. The whole phase space seems to be composed of all regular Kolmogorov–Arnold–Moser (KAM) curves. These regular curves can be generally classified into two types, the type that can intercept the horizontal line that separates prograde orbits from retrograde ones (such as example 1), and the type that cannot. None of these curves are chaotic. It seems difficult to understand the regular flip orbit as example 1, which according to the third frame in the left column of Figure 10 is not trapped by either the resonance $\psi_{1,-1} = 0$ or the resonance $\psi_{1,1} = 0$. We can interpret its existence as the regular KAM curves encompassing both resonance islands. A more intuitive picture showing its existence is given in Figure 14(b). Although two types of trajectories exist, we can take the whole space enveloped by the red curve shown in Figure 13(a) as a resonance island. Increasing the Hamiltonian value to the one corresponding to example 2, Figure 13(b) shows the corresponding surface of section. In this case, the same resonance island as the one shown in Figure 13(a) still exists. Meanwhile, the resonance island $\psi_{1,-1} = \pi$ gradually appears. The mutual influence of the two resonances causes the splitting of the

separatrix separating them and the occurrence of chaotic layer (Chirikov 1979); the trajectory of example 2 resides in this chaotic layer. Further increasing the Hamiltonian to the value of Figure 13(c), the resonance island $\psi_{1,-1} = \pi$ becomes more dominant and the chaotic layer separating the two resonance islands becomes thicker. Meanwhile, the resonance island $\psi_{1,1} = 0$ becomes obvious. With the Hamiltonian further increasing, the same resonance island as the one in Figure 13(a) completely disappears, and now the battle is between the resonances $\psi_{1,-1} = \pi$ and $\psi_{1,1} = 0$.

To conclude, for the inner orbit near-planar flip, we find two types of trajectories. One type is regular, as in example 1, which encompasses both resonances $\psi_{1,-1} = 0$ and $\psi_{1,1} = 0$ but is not trapped by either of them. The other type is chaotic due to overlap of different resonances, as in example 2.

Figure 14 presents the surfaces of section in the case of the inner orbit flip for another set of system parameters based on the exoplanet system HD 4113 (Tamuz et al. 2008; Cheetham et al. 2018).⁶ The ratio of masses, i.e., $m_1/m_2 = 0.02436$ indicates that m_1 is nonnegligible compared to the third companion m_2 . When the Hamiltonian is low, the surface in frame (a) presents a single resonance island which is similar to Figure 13(a). The red dots in frame (a) highlight a regular near-planar flip orbit along which i_{tot} can vary in $[5^\circ, 174^\circ]$. As the Hamiltonian increases, the chaotic near-planar inner orbit flip as presented in Figure 13(b) is not found. Further increasing the Hamiltonian to the value of Figure 14(b), the resonance centers $\psi_{1,-1} = 0$ and $\psi_{1,1} = 0$ both show up. The red dots highlight one of the regular KAM curves

⁵ If we choose the section $g_2 = \text{const}$ in the case of the inner orbit flip, the flow trapped in the resonance $\psi_{1,-1}/\psi_{1,1}$ will intersect the section in the positive/negative direction. In this way, for a flip orbit, we will get two surfaces instead of one, which may be inconvenient to study.

⁶ Table 6 in Cheetham et al. (2018) presented the astrometric orbital parameters of the planet HD 4113Ab and the third companion HD 4113C with respect to the stellar host HD 4113A. It was pointed out there that the inclination i_{Ab} and the longitude of the ascending node Ω_{Ab} of HD 4113Ab are unconstrained by the observation. Let i_C and Ω_C be the inclination and the longitude of the ascending node of HD 4113C. We take $i_{Ab} = 88^\circ \approx i_C$ and $\Omega_{Ab} = \Omega_C$ so that the system has an initially near-planar configuration. The derived orbital parameters in the Jacobi frame of the planet system HD 4113 are $m_0 = 1$, $m_1 = 1.449243 \times 10^{-3}$, $m_2 = 5.948947 \times 10^{-2}$, $a_1 = 1.298$, $a_2 = 23.72618$, $e_1 = 0.8999$, $e_2 = 0.4573286$, $i_1 = 2^\circ.110674$, $i_2 = 0^\circ.0060602$, $h_1 = -31^\circ.62401$, $h_2 = 148^\circ.3760$, $g_1 = 73^\circ.12860$, and $g_2 = 139^\circ.2049$ with the averaged Hamiltonian $\bar{H} = -8.784517 \times 10^{-9}$ and the normalized total angular momentum $\tilde{J} = 0.8866574$. This set of system parameters is partially used in Figure 14.

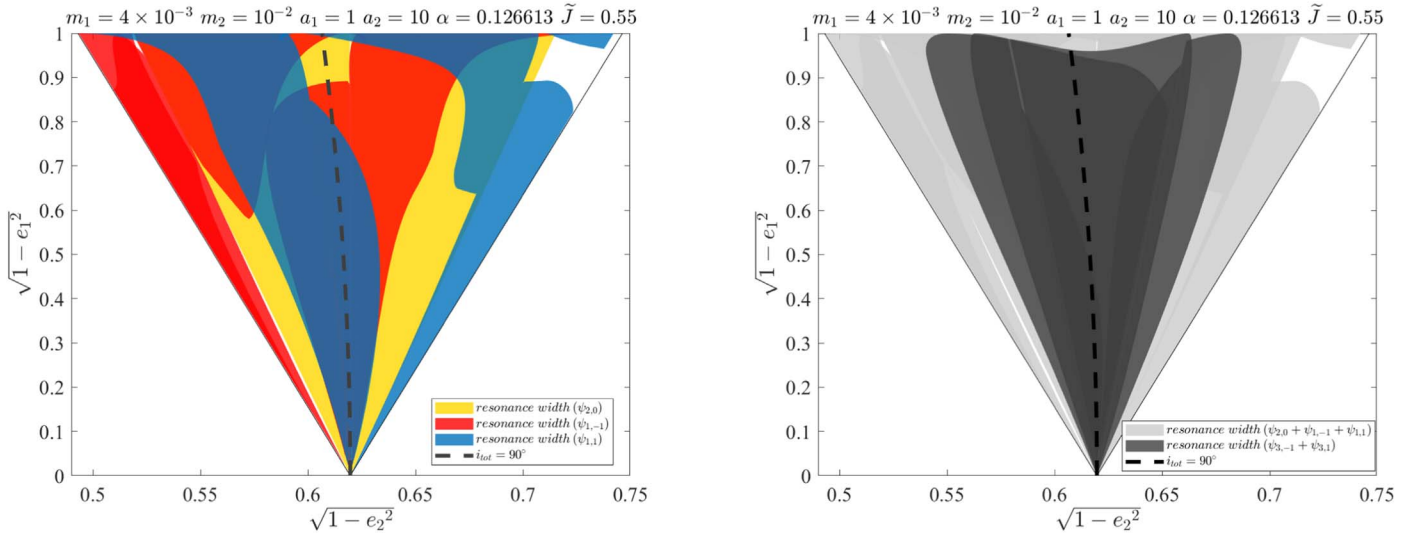


Figure 12. The resonance width of multiple resonances on the $\tilde{e}_1 - \tilde{e}_2$ plane in the case of inner orbit flip. Left: the yellow region corresponds to the resonance $\psi_{2,0}$ (also see the upper-left frame of Figure 1). The red region corresponds to the resonance $\psi_{1,-1}$ (also see the left frame of Figure 3). The blue region corresponds to the resonance $\psi_{1,1}$ (also see the left frame of Figure 6). Right: the dark-gray regions correspond to the resonances $\psi_{3,-1}$ and $\psi_{3,1}$, which have been presented in the left frames of Figures 7 and 8.

which envelop these two resonances but are not trapped by either of them. As the Hamiltonian increases to the positive value of Figure 14(c), the surface is dominated again by the single resonance island as in frame (a), and the motion is generally chaotic outside the resonance island. The red dots in frame (c) highlight a regular flip orbit along which i_{tot} can vary in $[38^\circ, 141^\circ]$. The surfaces in Figure 14 can be compared with Figure 4 of Li et al. (2014b), which was obtained under the inner test particle approximation. One remark is that in the cases exploited by us, the regular KAM curves highlighted in frame (b) generally break and no longer exist when m_1 and m_2 are comparable in the nonrestricted problem.

In the case of the outer orbit flip, the surfaces of section are presented in Figure 15. Different from the case of the inner orbit flip, only a chaotic flip of orbit is found because of the overlap of resonances $\psi_{1,-1}$ and $\psi_{1,1}$ and other resonance terms as discussed in Section 5.2.2. Frame (a) shows that even if the energy is very low, the resonance islands of $\psi_{1,-1} = 0$ and $\psi_{1,1} = 0$ both show up, and the chaotic flip orbits that migrate between these two resonances also show up. As the energy grows, the surfaces in frames (b) and (c) are generally similar to frame (a). The mutual inclination i_{tot} along the chaotic flip orbit marked with red dots in frame (a) can vary in $[2^\circ, 170^\circ]$ while i_{tot} can vary in $[2^\circ, 150^\circ]$ in frame (b). The intersection points of example 3 are marked with red dots on the surface in frame (c). To conclude, for the outer orbit near-planar flip and the cases we studied, the regular near-planar flip orbit as in example 1 does not exist, and only the chaotic near-planar flip orbit as in example 3 exists. The results obtained here can be compared with Naoz et al. (2017) where both regular and chaotic flips of the outer orbit were found in the restricted problem.

6. Conclusion

In this paper, secular resonances in nonrestricted hierarchical triple systems were investigated. The properties of equilibrium points, i.e., number, location, stability, and resonance width, for each secular resonant term were first investigated. The resonances introduce large-amplitude variations in the orbit eccentricity or the inclination, and thus lead to some extraordinary dynamical

behaviors, such as the phenomenon that the orbit eccentricity goes from near zero to almost unity and the phenomenon of orbit flip with near-perpendicular configuration of the inner and the outer orbit. After treating with each single resonance term separately, we combine them together to study the general secular dynamics of the nonrestricted system, with a special focus on the near-planar orbit flip. We find that only the joint effects of different resonance terms can generate the near-planar orbit flip.

In Section 2.1, the nine-DOF Hamiltonian of the original spatial three-body problem was reduced to Harrington's Hamiltonian using the Jacobi coordinate. We showed that the invariable plane could be naturally derived from the definition of the elimination of nodes, i.e., the relation $h_1 - h_2 = \pi$, without the need for the quadrupole approximation or the double-averaging process. The disturbing function with the nodes eliminated was fully developed using Kaula's (1961) method. The explicit expression of the double-averaged Hamiltonian truncated at the octupole order was presented.

The theory on the quadrupole term was reformulated in Section 3. The equilibrium points of $\psi_{2,0} = \pi$ were solved as a quadratic equation. The roots of the quadratic equation were used to derive the criterion for the prograde-retrograde state of the equilibrium point. A necessary but insufficient condition for the orbit flip due to the quadrupole term was presented. The resonance width was determined and for the first time displayed on the $\tilde{e}_1 - \tilde{e}_2$ plane.

In Section 4, all four resonant octupole terms were investigated. The resonances $\psi_{1,-1}$ and $\psi_{1,1}$ dominate other resonance terms in the near-planar configuration. The inner orbit eccentricity and the outer orbit eccentricity vary in opposite directions when influenced by these two terms. In some cases, the orbit eccentricities can even reach almost unity. The resonances $\psi_{3,-1}$ and $\psi_{3,1}$ are weaker because their strength is proportional to $e_1^3 e_2$ and only matters when the orbit eccentricities are large enough. Different from the resonance terms $\psi_{1,-1}$ and $\psi_{1,1}$, they are only obvious when the inner and outer orbits have a near-perpendicular configuration. The resonance widths of four octupole resonant terms were numerically determined and displayed on the $\tilde{e}_1 - \tilde{e}_2$ plane. For each of them, we found that the orbit flip is possible.

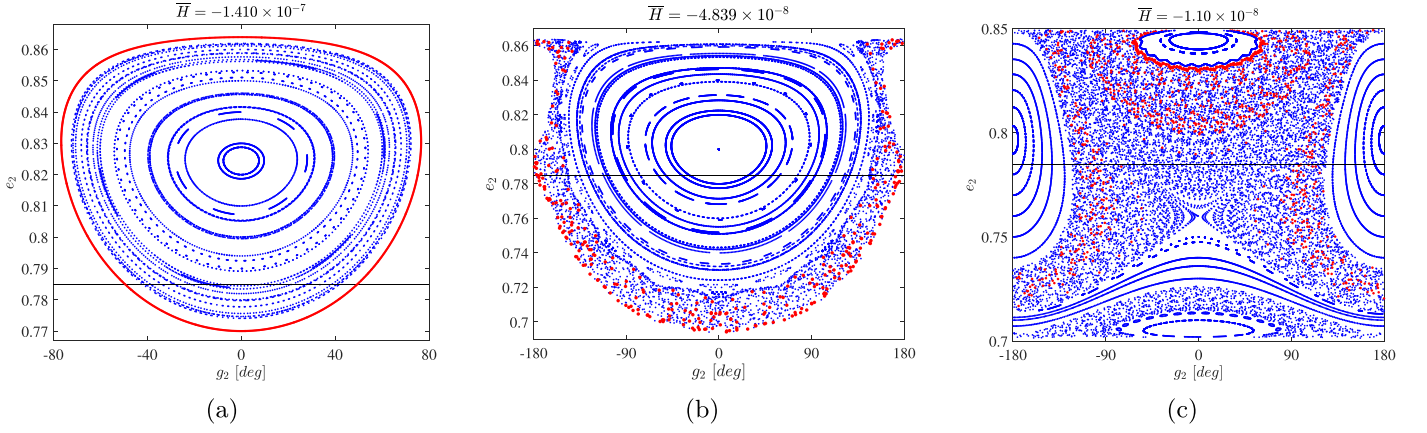


Figure 13. The surfaces of section $g_1 = 0$ in the case of the inner orbit flip. The system parameters are ($m_1 = 4 \times 10^{-3}$, $m_2 = 10^{-2}$, $a_1 = 1$, $a_2 = 10$, $\bar{J} = 0.55$) with $\alpha = 0.12661$. The horizontal solid line is determined by $e_2 = \sqrt{1 - (1 + \alpha)^2 \bar{J}^2}$, which is the intersection point of $i_{\text{tot}} = 90^\circ$ and $e_1 = 1$. As shown in the left frame of Figure 12, this point is where the separatrices of two single resonances $\psi_{1,-1}$ and $\psi_{1,1}$ touch for the near-planar configuration. In this way, the horizontal straight line on the surface approximately separates prograde orbits from retrograde orbits. Generally, the orbit that crosses this line on the surface will flip. The red dots in frame (a) highlight the intersections points of example 1. The red dots in frame (b) highlight the intersections points of example 2. The red dots in frame (c) highlight one of the chaotic flip orbits along which i_{tot} can vary in $[30^\circ, 150^\circ]$.

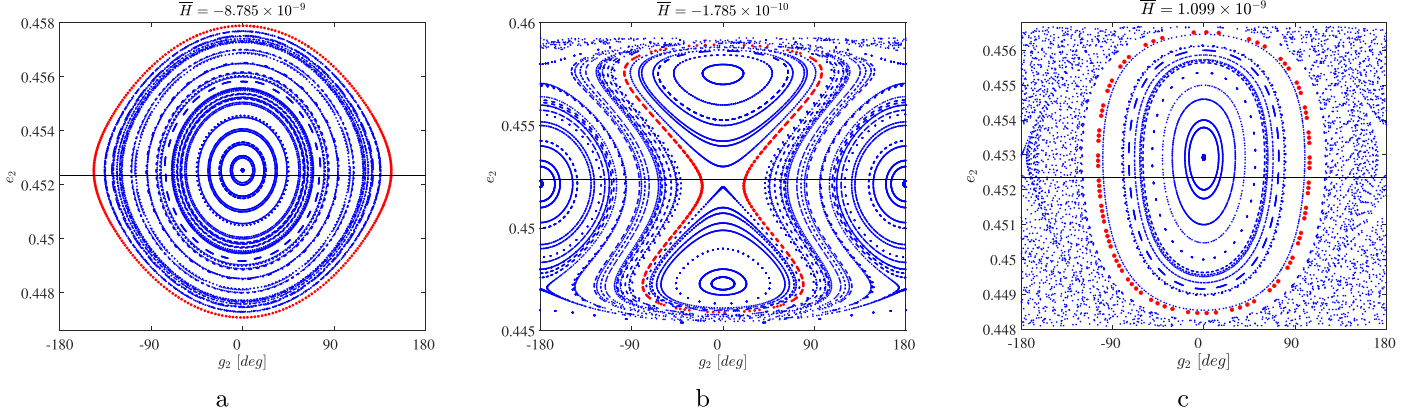


Figure 14. The surfaces of section $g_2 = 0$ in the case of inner orbit flip. The system parameters are ($m_1 = 1.449243 \times 10^{-3}$, $m_2 = 5.948946 \times 10^{-2}$, $a_1 = 1.298$, $a_2 = 23.72618$, $\bar{J} = 0.8866574$) with $\alpha = 5.843 \times 10^{-3}$, which are derived from the orbital parameters of the exoplanetary system HD 4113. The horizontal solid line is determined by $e_2 = \sqrt{1 - (1 + \alpha)^2 \bar{J}^2}$.

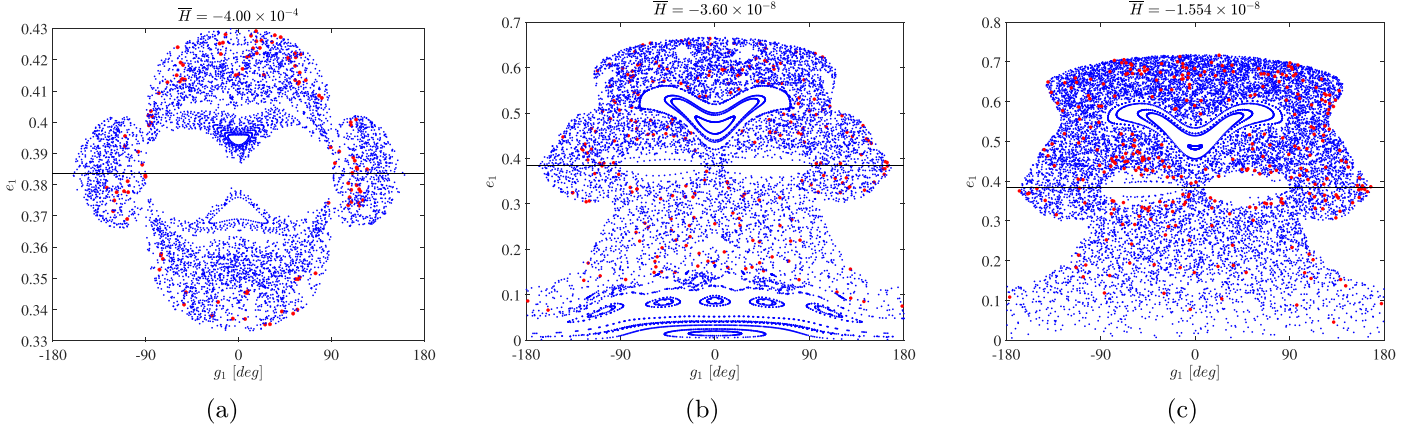


Figure 15. The surfaces of section $g_2 = 0$ in the case of the outer orbit flip. The system parameters are ($m_1 = 10^{-2}$, $m_2 = 10^{-3}$, $a_1 = 1$, $a_2 = 10$, $\bar{J} = 0.7$) with $\alpha = 3.1325$. The horizontal solid line is determined by $e_1 = \sqrt{1 - \frac{(1 + \alpha)^2 \bar{J}^2}{\alpha^2}}$, which is the intersection point of $i_{\text{tot}} = 90^\circ$ and $e_2 = 1$.

However, all orbit flips caused by a single resonance (including the quadrupole term) only happens for the near-perpendicular configuration of the inner and the outer orbits.

In Section 5, the full averaged Hamiltonian truncated at the octupole level was studied, with a special focus on the phenomenon of orbit flip. With the aid of three examples, we intuitively showed readers two types of near-planar flip orbits. One type is regular and the other type is chaotic. The regular type of near-planar flip orbit can be viewed as a special type of regular orbits which encompass both the resonance islands $\psi_{1,-1}$ and $\psi_{1,1}$

$$\begin{aligned} \frac{dh_1}{dt} - \frac{dh_2}{dt} &= \frac{\partial H}{\partial H_1} - \frac{\partial H}{\partial H_2} = \sum_{l=2}^{\infty} \alpha_n \frac{r_1^l}{r_2^{l+1}} \frac{\partial P_l(\cos \Phi)}{\partial \cos \Psi} \\ &\times \begin{cases} \sin u_1 \sin u_2 \left(\cos \theta \cos i_2 - \frac{\cos i_1}{\sin i_1} \sin i_2 \right) \frac{1}{G_1} \\ -\sin u_1 \sin u_2 \left(\cos \theta \cos i_1 - \frac{\cos i_2}{\sin i_2} \sin i_1 \right) \frac{1}{G_2} \\ -\sin u_1 \cos u_2 \frac{\sin \theta}{G_1} + \cos u_1 \sin u_2 \frac{\sin \theta}{G_2} \end{cases} \end{aligned} \quad (\text{A2})$$

but are not trapped by either of them (see Figures 13(a) and 14(c)). This type of flip orbit only exists in the full averaged Hamiltonian. The chaotic type of near-planar flip orbit is due to the overlap of different resonances and resides in the chaotic layers separating these resonances. Using the tool of surface of section, we were able to clearly show the difference between the two types of flip orbits in phase space. For the cases we studied, we found both types of flip orbits existed for the inner orbit flip, but only the chaotic type of flip orbits existed for the outer orbit flip.

Based on the nonrestricted secular octupole perturbation theory, the phase space where the planet system HD 4113 dwells in was investigated. The results in Figure 14 showed that the dynamics introduced by the secular octupole terms may play a key role in the long-term evolution of the planet system HD 4113. The highly eccentric orbit of HD 4113Ab can be explained by the dominating resonance $\psi_{1,-1}$ with the near-planar configuration of the system. The interactions of multiple secular resonant terms can lead to the dramatic growth of mutual inclination and the near-planar flip of the orbit. This near-planar flip of orbit is regular, as discussed in Section 5. Like the exoplanetary system HD 4113, it is believed that the nonrestricted octupole perturbation theory may be applied to a wider range of natural hierarchical systems where the mass of each member is nonnegligible.

This work is supported by the National Natural Science Foundation of China (11973010, 11773017).

Appendix A Introduction of the Invariable Plane

Naoz et al. (2013) pointed out that the elimination of nodes should be conducted on the level of the equations of motion instead of the Hamiltonian, otherwise one may be led to the wrong conclusion that the vertical component of the inner orbit's angular momentum is conserved. We note that this problem can be overcome with the use of Delapierre elements in the process of the elimination of nodes (Ferrer & Osacar 1994; Palacian et al. 2013). Here, we show that the definition of the invariable plane can be naturally derived from the equations of motion with the condition $\theta = h_1 - h_2 = \text{const}$. We note that this process does not depend on the quadrupole approximation or the double-averaged

approximation of the system. The cosine of the angle Φ can be expressed in terms of the orbital elements as follows:

$$\begin{aligned} \cos \Phi &= \cos \theta \cos u_1 \cos u_2 + \sin \theta \cos u_1 \\ &\times \sin u_2 \cos i_2 - \sin \theta \cos u_2 \sin u_1 \cos i_1 \\ &+ \cos \theta \sin u_1 \sin u_2 \cos i_1 \cos i_2 \\ &+ \sin u_1 \sin u_2 \sin i_1 \sin i_2, \end{aligned} \quad (\text{A1})$$

where $u = f + g$ and f is the true anomaly of the orbit. As the Hamiltonian only depends on the conjugated momentum H_i through $\cos \Phi$, we have

Taking the assumption that the orbital phases, i.e., u_1 and u_2 , are random, then the condition $\theta = h_1 - h_2 = \text{const}$ suggests that

$$\begin{aligned} G_1 \left(\cos \theta \cos i_1 - \frac{\cos i_2}{\sin i_2} \sin i_1 \right) \\ = G_2 \left(\cos \theta \cos i_2 - \frac{\cos i_1}{\sin i_1} \sin i_2 \right), \end{aligned} \quad (\text{A3})$$

$$\theta = 0 \text{ or } \pi. \quad (\text{A4})$$

Substituting Equation (A4) into Equation (A3), one may find that

$$G_1 \sin i_1 = -G_2 \sin i_2 \quad \text{when } \theta = 0, \quad (\text{A5})$$

$$G_1 \sin i_1 = G_2 \sin i_2 \quad \text{when } \theta = \pi. \quad (\text{A6})$$

If we assume that the inclination is defined within the range $[0, \pi]$, then only Equation (A6) holds. It is not hard to find that the angular momentum \mathbf{J}_i of m_i is defined as follows:

$$\mathbf{J}_j = \tilde{m}_j \sqrt{\mu_1 a_1 (1 - e_1^2)} \begin{pmatrix} \sin h_j \sin i_j \\ -\cos h_j \sin i_j \\ \cos i_j \end{pmatrix}. \quad (\text{A7})$$

Using Equations (A6) and (A7), one may find that the projections of the total angular momentum vector, i.e., $\mathbf{J} = \mathbf{J}_1 + \mathbf{J}_2$, on the x -axis and y -axis both equal zero, which suggests that \mathbf{J} is perpendicular to the x - y plane, and this is exactly the definition of the invariable plane. The conservation of \mathbf{J} guarantees that the condition $\theta = h_1 - h_2 = \pi$ holds all the time if the z -axis is initially set along the direction of \mathbf{J} .

It is obvious that the constraint presented by Equation (7) can be easily derived from Equation (A6) and the constraint by Equation (8) holds because of the conservation of the magnitude of the angular momentum, i.e., $\mathbf{J} \cdot \mathbf{z} = \text{const}$.

Appendix B Quadrupole Criterion

It can be shown that $\xi_1 < 0$ (see Section B.1 for details), which naturally gives $\xi_1 - \alpha^2\eta < 0$. According to Equation (11), one may easily see that $\cos i_{\text{tot}}|_{\xi_1} < 0$. Notice that by the definition of ξ , $\xi < 0 \iff \tilde{J} < \sqrt{1 - e_2^2}/1 + \alpha$. So, the equilibrium point for the resonance $\psi_{2,0} = \pi$ is in retrograde state when $\tilde{J} < \sqrt{1 - e_2^2}/1 + \alpha$. Also it is obvious that $\xi_2 > 0$ by its definition and $\xi > 0 \iff \tilde{J} > \sqrt{1 - e_2^2}/1 + \alpha$. It can be shown that $\cos i_{\text{tot}}|_{\xi_2} > 0$ (see Section B.2 for details). As a result, the equilibrium point for the resonance $\psi_{2,0} = \pi$ is in prograde state when $\tilde{J} > \sqrt{1 - e_2^2}/1 + \alpha$.

B.1. Proof 1

Supposing that $\xi_1 > 0$, Equation (32) requires that $\eta > \eta_c = \frac{5}{8} + \frac{3\beta}{2\alpha^2}$, which naturally gives $\beta/\alpha^2 < 1/4$. We show that this assumption will lead to $\cos i_1 > 1$, which is an obvious error.

First, we calculate the value of $\cos i_1$ when $\eta = \eta_c$,

$$\begin{aligned} \cos i_1|_{\eta=\eta_c, \xi_1=0} &= \frac{\alpha^2\eta_c}{2\alpha\sqrt{\beta\eta_c}} \\ &= \sqrt{\frac{3}{8} + \frac{5}{32}\frac{\alpha^2}{\beta}} > \sqrt{\frac{3}{8} + \frac{5}{32}} \times 4 = 1. \end{aligned} \quad (\text{B1})$$

Then, when $\eta = 1$ we have

$$\begin{aligned} \cos i_1|_{\eta=1} &= \frac{\xi_1 + \alpha^2}{2\alpha\sqrt{\xi + \beta}} \Big|_{\eta=1} \\ &= \frac{9 - y}{10\sqrt{\frac{4-y}{5} + \frac{1}{60}(y^2 - 1)}} := f(y), \end{aligned} \quad (\text{B2})$$

where $y = \sqrt{1 + 60\frac{\beta}{\alpha^2}} \in (1, 4)$. It is easy to calculate that

$$\frac{df(y)}{dy} = \frac{-\frac{1}{2}(y - \frac{7}{3})}{100\left(\frac{4-y}{5} + \frac{1}{60}(y^2 - 1)\right)^{\frac{3}{2}}}, \quad f(1) = \sqrt{16/15}, \quad \text{and} \quad f(4) = 1,$$

which suggests that $\cos i_1|_{\eta=1} > 1$. From the intermediate value theorem, as $\cos i_1|_{\eta=1}$ or $\eta_c > 1$, if $\exists \eta_0 \in (\eta_c, 1)$ such that $\cos i_1|_{\eta_0} < 1$, then $\exists \eta_0 \in (\eta_c, 1)$ such that $\cos i_1|_{\eta_0} = 1$. Applying $\cos i_1|_{\eta_0} = 1$ to Equation (9), one may obtain that

$$\xi^2 - 2\alpha^2\eta_0\xi + \alpha^4\eta_0^2 - 4\alpha^2\beta\eta_0 = 0. \quad (\text{B3})$$

The roots of Equation (B3) are $\xi = \alpha^2\eta \pm 2\alpha\sqrt{\beta\eta}$. Because $\xi_1 - \alpha^2\eta < 0$, then we have $\xi_1 = \alpha^2\eta - 2\alpha\sqrt{\beta\eta}$, which is equivalent to the following equation:

$$g(\eta) := \sqrt{\eta} \left(5 - 4\eta + \sqrt{(4\eta - 5)^2 + 60\frac{\beta}{\alpha^2}} \right) = 10\sqrt{\frac{\beta}{\alpha^2}}. \quad (\text{B4})$$

Now we prove that Equation (B4) has no root. The first derivative of $g(\eta)$ is

$$\frac{dg(\eta)}{d\eta} = \frac{-h(x, \varepsilon) + \varepsilon}{2\sqrt{\eta}\sqrt{(4\eta - 5)^2 + 60\frac{\beta}{\alpha^2}}}, \quad (\text{B5})$$

where $h(x) = (10 - 3x)(\sqrt{x^2 + \varepsilon} + x)$, $\varepsilon = 60\frac{\beta}{\alpha^2} < 15$ and $x = 5 - 4\eta \in \left(1, \frac{5}{2} - \frac{6\beta}{\alpha^2}\right)$. The first derivative of $h(x)$ is

$$\frac{dh(x)}{dx} = -3(x + \sqrt{x^2 + \varepsilon}) \left(\frac{x + \sqrt{x^2 + \varepsilon} - \frac{10}{3}}{\sqrt{x^2 + \varepsilon}} \right), \quad (\text{B6})$$

which suggests that $h(x)_{\min} = \min \left\{ h(1), h\left(\frac{5}{2} - \frac{6\beta}{\alpha^2}\right) \right\}$, and it is easy to verify that $h(1) = 7(\sqrt{1 + \varepsilon} + 1) > \varepsilon$ and $h\left(\frac{5}{2} - \frac{6\beta}{\alpha^2}\right) = \left(\frac{5}{2} + \frac{3}{10}\varepsilon\right) \left(\sqrt{\left(\frac{5}{2} - \frac{3}{10}\varepsilon\right)^2 + \left(\frac{5}{2} - \frac{3}{10}\varepsilon\right)} \right) > \varepsilon$ when $\varepsilon < 15$, which shows that $h(x) > \varepsilon$, hence $dg(\eta)/d\eta < 0$, then $g(\eta)_{\min} = g(1)$. It is easy to verify that $g(1) - 10\frac{\beta}{\alpha^2} = \left(1 + \sqrt{1 + 60\frac{\beta}{\alpha^2}}\right) - 10\frac{\beta}{\alpha^2} > 0$ when $\beta/\alpha^2 < 1/4$. ■

B.2. Proof 2

From Equations (10) and (12), we have

$$\frac{\sin i_{\text{tot}}}{\sin i_1} \cos i_2 = \frac{\xi - \alpha^2\eta + 2\beta}{2\beta}. \quad (\text{B7})$$

Substituting Equation (B7) into Equation (30), we have

$$\eta - 5(1 - \cos^2 i_{\text{tot}}) + (5 - 4\eta) \frac{\xi - \alpha^2\eta + 2\beta}{2\beta} = 0. \quad (\text{B8})$$

From Equation (11), we have

$$\xi - \alpha^2\eta = 2\alpha\sqrt{\eta\beta} \cos i_{\text{tot}}. \quad (\text{B9})$$

Substituting Equation (B9) into Equation (B8), we have

$$(\alpha\sqrt{\beta\eta}(5 - 4\eta)) \cos i_{\text{tot}} = \beta(3\eta - 5 \cos^2 i_{\text{tot}}). \quad (\text{B10})$$

From Equation (B10), one may easily verify that the following relations hold:

$$\eta = 0 \iff i_{\text{tot}} = 90^\circ, \quad (\text{B11})$$

$$i_{\text{tot}} < 90^\circ \iff 3\eta > 5 \cos^2 i_{\text{tot}}, \quad (\text{B12})$$

$$i_{\text{tot}} > 90^\circ \iff 3\eta < 5 \cos^2 i_{\text{tot}}, \quad (\text{B13})$$

where \iff means ‘‘if and only if’’. To determine the sign of $\cos i_{\text{tot}}|_{\xi_2}$, we only need to calculate the value of

$5 \cos^2 i_{\text{tot}}|_{\xi_2} - 3\eta$. From Equations (11) and (33), we have

$$\begin{aligned}
5 \cos^2 i_{\text{tot}}|_{\xi_2} - 3\eta &= \frac{5\alpha^2\eta}{4\beta} \left(\frac{4\eta - 5 + \sqrt{\Delta}}{5} \right)^2 \\
- 3\eta &= \frac{5\alpha^2\eta}{4\beta} \left(\left(\frac{4\eta - 5 + \sqrt{\Delta}}{5} \right)^2 - \frac{12\beta}{5\alpha^2} \right) \\
&= \frac{5\alpha^2\eta}{4\beta} \left(\left(\frac{4}{5}\eta - 1 \right)^2 + \frac{\Delta}{25} + 2 \left(\frac{4}{5}\eta - 1 \right) \frac{\sqrt{\Delta}}{5} - \frac{12\beta}{5\alpha^2} \right) \\
&= \frac{5\alpha^2\eta}{4\beta} \left(\left(\frac{4}{5}\eta - 1 \right)^2 + \frac{(4\eta - 5)^2 + 60\frac{\beta}{\alpha^2}}{25} \right. \\
&\quad \left. + 2 \left(\frac{4}{5}\eta - 1 \right) \frac{\sqrt{\Delta}}{5} - \frac{12\beta}{5\alpha^2} \right) \\
&= \frac{5\alpha^2\eta}{4\beta} \left(2 \left(\frac{4}{5}\eta - 1 \right)^2 \right. \\
&\quad \left. + 2 \left(\frac{4}{5}\eta - 1 \right) \frac{\sqrt{\Delta}}{5} \right) \\
&= -\frac{5\alpha^2\eta}{2\beta} \left(1 - \frac{4}{5}\eta \right) \frac{\sqrt{(5-4\eta)^2 + 60\frac{\beta}{\alpha^2}} - (5-4\eta)}{5} < 0.
\end{aligned}$$

From Equation (B12), it is obvious that $\cos i_{\text{tot}}|_{\xi_2} > 0$. ■

Appendix C Special Equilibrium

It is obvious from Equation (31) that $\eta = 0 \implies \xi = 0$. Substituting $\xi = 0$ into Equation (31), we have

$$\eta^2 \left(\eta - \frac{5}{8} - \frac{3\beta}{2\alpha^2} \right) = 0, \quad (\text{C1})$$

which gives $\eta = 0$ or $\eta = \frac{5}{8} + \frac{3\beta}{2\alpha^2}$. Supposing $\eta = \frac{5}{8} + \frac{3\beta}{2\alpha^2}$ holds, we have

$$e_1^2 = 1 - \eta = \frac{3}{8} - \frac{3\beta}{2\alpha^2} \geq 0 \implies \frac{\beta}{\alpha^2} \leq \frac{1}{4}. \quad (\text{C2})$$

Substituting $\eta = \frac{5}{8} + \frac{3\beta}{2\alpha^2}$ and $\xi = 0$ into Equation (9), one may obtain

$$\cos i_1 = \frac{\alpha^2\eta}{2\alpha\sqrt{\beta\eta}} \leq 1 \implies \eta \leq 4\frac{\beta}{\alpha^2} \implies \frac{\beta}{\alpha^2} \geq \frac{1}{4}. \quad (\text{C3})$$

Equations (C2) and (C3) imply that $\beta = \alpha^2/4$ must hold, which gives $\eta = 1$. Substituting $\eta = 1$ and $\xi = 0$ into Equations (9) and (10), it is easy to see that $i_1 = 0$ and $i_2 = \pi$. This is the planar situation where the Hamiltonian of the quadrupole term is zero and will not be considered here. Thus, $\eta = 0$ must hold. As a result, we have shown that $\eta = 0 \Leftrightarrow \xi = 0$. Further, one may see that $\xi = 0 \implies i_1 = 90^\circ$ from Equations (12) and (B11). Now, it can be concluded that

$$\tilde{J} = \frac{\sqrt{1-e_2^2}}{1+\alpha} \Leftrightarrow e_1 = 1 \Leftrightarrow i_1 = 90^\circ \text{ and } i_2 = 0. \quad (\text{C4})$$

■

Appendix D Three Roots

$$\text{root}_1 = -\frac{P}{24 \cdot 2^{2/3} c^2 Q} + \frac{Q}{48 \sqrt[3]{2} c^2} + \frac{T}{12c^2}, \quad (\text{D1})$$

$$\text{root}_2 = \frac{(1+i\sqrt{3})P}{48 \cdot 2^{2/3} c^2 Q} - \frac{(1-i\sqrt{3})Q}{96 \sqrt[3]{2} c^2} + \frac{T}{12c^2}, \quad (\text{D2})$$

$$\text{root}_3 = \frac{(1-i\sqrt{3})P}{48 \cdot 2^{2/3} c^2 Q} - \frac{(1+i\sqrt{3})Q}{96 \sqrt[3]{2} c^2} + \frac{T}{12c^2}, \quad (\text{D3})$$

where

$$c = \frac{\alpha}{2\sqrt{\beta}}, \quad d = \frac{\xi}{2\alpha\sqrt{\beta}}, \quad \tilde{E} = \frac{8}{3} \left(E - \frac{5}{32} \right),$$

$$T = 5c^2 + 8cd + 3,$$

$$P = 48c^2(40cd + 16d^2 + 4\tilde{E} + 15)$$

$$- 16T^2, \quad Q = \sqrt[3]{\sqrt{4P^3 + S^2} + S},$$

$$\begin{aligned}
S &= 16000c^6 - 38400c^5d + 30720c^4d^2 - 11520c^4\tilde{E} \\
&\quad - 14400c^4 - 8192c^3d^3 - 18432c^3d\tilde{E} \\
&\quad - 46080c^3d + 46080c^2d^2 - 6912c^2\tilde{E} \\
&\quad - 8640c^2 + 27648cd + 3456.
\end{aligned}$$

Appendix E

Analytical Expression for the Resonance Width of $\psi_{2,0}$

When the necessary condition for the orbit to flip at the quadrupole approximation, namely Equation (42), is satisfied, the energy for the separatrix between circulation and libration is as follows:

$$E = \begin{cases} (1) \frac{5c^2 - 6cd - 3}{8c^2}, & \text{if } \beta \leq \theta^2 \leq \alpha^2 - 3\beta, \\ (2) \frac{3(d-c)^2 - 1}{8}, & \text{if } \alpha^2 - 3\beta \leq \theta^2 \leq \alpha^2 + \beta. \end{cases} \quad (\text{E1})$$

We briefly explain how the above expression is obtained. In case (1), we know that the saddle at $g = 0$ exits according to Section 3.1. Then, the energy of the separatrix is given by the energy of the saddle, which is $\bar{E} = -\frac{1+2cd}{c^2}$. Case (2) corresponds to region II' of the Figure 1 in Lidov & Ziglin (1976) and the energy of the separatrix is given by Equation (41) there. Then, the maximum range of e_1 determined by the separatrix is as follows:

$$(e_{1,\min}, e_{1,\max}) = (\sqrt{1 - \text{root}_2}, \sqrt{1 - \text{root}_3}). \quad (\text{E2})$$

ORCID iDs

Xinhao Liao  <https://orcid.org/0000-0003-4168-5061>

References

- Albrecht, S., Winn, J. N., Johnson, J. A., et al. 2012, *ApJ*, 757, 18
 Cheetham, A., Segransan, D., Peretti, S., et al. 2018, *A&A*, 614, A16
 Chirikov, B. V. 1979, *PhR*, 52, 263
 Dawson, R. I., & Johnson, J. A. 2018, *ARA&A*, 56, 175
 Deprit, A. 1983, *CeMec*, 30, 181
 Ferrer, S., & Osacar, C. 1994, *CeMDA*, 58, 245
 Ford, E. B., Kozinsky, B., & Rasio, F. A. 2000, *ApJ*, 535, 385

- Harrington, R. S. 1968, *AJ*, **73**, 190
- Ji, J., Kinoshita, H., Liu, L., Li, G., & Nakai, H. 2003, *CeMDA*, **87**, 113
- Katz, B., Dong, S., & Malhotra, R. 2011, *PhRvL*, **107**, 181101
- Kaula, W. M. 1961, *GeoJI*, **5**, 104
- Kinoshita, H., & Nakai, H. 2007, *CeMDA*, **98**, 67
- Kozai, Y. 1962, *AJ*, **67**, 591
- Lee, M. H., & Peale, S. J. 2003, *ApJ*, **592**, 1201
- Li, G., Naoz, S., Holman, M. J., & Loeb, A. 2014a, *ApJ*, **791**, 86
- Li, G., Naoz, S., Kocsis, B., & Loeb, A. 2014b, *ApJ*, **785**, 116
- Lidov, M. L. 1962, *P&SS*, **9**, 719
- Lidov, M. L., & Ziglin, S. L. 1976, *CeMec*, **13**, 471
- Lithwick, Y., & Naoz, S. 2011, *ApJ*, **742**, 94
- Martin, D. V., & Triaud, A. H. M. J. 2016, *MNRAS*, **455**, L46
- Naoz, S. 2016, *ARA&A*, **54**, 441
- Naoz, S., Farr, W. M., Lithwick, Y., Rasio, F. A., & Teyssandier, J. 2011, *Natur*, **473**, 187
- Naoz, S., Farr, W. M., Lithwick, Y., Rasio, F. A., & Teyssandier, J. 2013, *MNRAS*, **431**, 2155
- Naoz, S., Li, G., Zanardi, M., de Elia, G. C., & Sisto, R. P. D. 2017, *AJ*, **154**, 18
- Palacian, J. F., Sayas, F., & Yanguas, P. 2013, *Qual. Theory Dyn. Syst.*, **12**, 143
- Tamuz, O., Segransan, D., Udry, S., et al. 2008, *A&A*, **480**, L33
- Vashkov'Yak, M. A. 1999, *AstL*, **25**, 476